MULTISCALE MODEL. SIMUL.
Vol. 6, No. 4, pp. 1317–1346

MULTISCALE ANALYSIS AND COMPUTATION FOR THE THREE-DIMENSIONAL INCOMPRESSIBLE NAVIER–STOKES EQUATIONS*

THOMAS Y. HOU†, DANPING YANG‡, AND HONGYU RAN†

Abstract. In this paper, we perform a systematic multiscale analysis for the three-dimensional incompressible Navier–Stokes equations with multiscale initial data. There are two main ingredients in our multiscale method. The first one is that we reparameterize the initial data in the Fourier space into a formal two-scale structure. The second one is the use of a nested multiscale expansion together with a multiscale phase function to characterize the propagation of the small-scale solution dynamically. By using these two techniques and performing a systematic multiscale analysis, we derive a multiscale model which couples the dynamics of the small-scale subgrid problem to the large-scale solution without a closure assumption or unknown parameters. Furthermore, we propose an adaptive multiscale computational method which has a complexity comparable to a dynamic Smagorinsky model. We demonstrate the accuracy of the multiscale model by comparing with direct numerical simulations for both two- and three-dimensional problems. In the two-dimensional case we consider decaying turbulence, while in the three-dimensional case we consider forced turbulence. Our numerical results show that our multiscale model not only captures the energy spectrum very accurately, it can also reproduce some of the important statistical properties that have been observed in experimental studies for fully developed turbulent flows.

Key words. multiscale analysis, turbulence modeling, three-dimensional Navier–Stokes equations

AMS subject classifications. Primary, 76M50, 76F05; Secondary, 76F65, 76M22

DOI. 10.1137/070682046

1. Introduction.

We develop a systematic multiscale analysis for the three-dimensional (3D) incompressible Navier–Stokes equations with multiscale initial data. The understanding of scale interactions for incompressible flows has been a major challenge. For high Reynolds number flows, the degrees of freedom are so large that it is almost impossible to resolve all small scales by direct numerical simulations. Deriving an effective equation for the large-scale solution is very useful for engineering applications. There have been some well-known large eddy simulation (LES) models available in the literature; see, e.g., [31, 24, 12, 11, 27, 18, 28]. However, many of the LES models are based on some closure assumptions which cannot be verified, and they contain unknown parameters. It would be desirable to derive a more systematic LES model which does not contain unknown parameters and can be justified by multiscale analysis. On the other hand, the nonlinear and nonlocal nature of the Navier–Stokes equations makes it difficult to perform multiscale analysis. One of the important questions is to understand how small scales are generated and propagate in time and whether the multiscale structure of the solution is preserved dynamically.

*Received by the editors February 7, 2007; accepted for publication (in revised form) September 20, 2007; published electronically March 26, 2008. This work was supported in part by the NSF under grant DMS-0073916 and ITR grant ACI-0204932.

http://www.siam.org/journals/mms/6-4/68204.html

†Applied and Computational Mathematics, 217-50, Caltech, Pasadena, CA 91125 (hou@acm.caltech.edu, hongy@its.caltech.edu).

‡Department of Mathematics, East China Normal University, Shanghai, 200062, China (dpyang@euler.math.ecnu.edu.cn). The work of this author was supported in part by the National Basic Research Program of the People's Republic of China under grant 2005CB321703 and under the NSFC grants 10571108 and 10441005.

Our multiscale analysis is motivated by the previous work of McLaughlin–Papanicolaou–Pironneau (MPP) on the 3D Euler equations using homogenization techniques [26]. To construct a multiscale expansion for the solution of the Euler equations, they made an important assumption that the oscillation is convected by the mean flow. By using multiscale expansion techniques, MPP obtained a periodic cell problem for the velocity field and the pressure. However, it is not clear whether the resulting cell problem has a solution that is periodic in both the fast space variable $\mathbf{y}$ and the fast time variable τ. Additional assumptions were imposed on the solution of the cell problem in order to derive a variant of the $k-\epsilon$ model. Inspired by the pioneering work of MPP [26], there have been many subsequent contributions in this area; see, e.g., [3, 8, 30, 2, 6, 7, 5].

In this paper, we generalize the multiscale analysis of MPP to problems with infinitely many nonseparated scales and develop a novel multiscale analysis for the incompressible Euler and Navier–Stokes equations. There are two key ingredients in our multiscale analysis. The first one is to reformulate the solution in the Fourier space into a formal two-scale structure. The second one is to introduce a multiscale phase function to characterize the propagation of the small scales. By using this new multiscale phase function, the two-scale structure of the initial condition is preserved dynamically. At the end, we derive a multiscale model which couples the dynamics of the small-scale subgrid problem to the large-scale solution. Further, we develop a simplified multiscale model in which only the average of the multiscale phase function is used in the multiscale expansion. This significantly simplifies the computation of the cell problems.

Based on the multiscale analysis we develop for the incompressible Euler equations, we have designed an effective multiscale computational method to solve the 3D incompressible Navier–Stokes equations. In order to reduce the computational cost, we design an effective adaptive method which updates only a small number of cell problems at each time step. This offers considerable computational savings. The adaptive multiscale method is much more efficient than a direct numerical simulation but is slightly more expensive than the Smagorinsky LES model [31, 12]. On the other hand, with only a modest extra computational cost compared with the LES model, our multiscale model offers better accuracy for the large-scale solution than the LES model and has the capability of computing some subgrid statistical properties which cannot be obtained by a LES model. Most importantly, our multiscale method has no unknown parameters, and we do not make any heuristic closure assumption.

We demonstrate the accuracy of our multiscale model in both two and three dimensions with random initial data. In the two-dimensional case, we test how well our multiscale model can capture the inverse cascade process from a random initial vorticity distribution. In the three-dimensional case, we test the accuracy of the multiscale model for the forced homogeneous turbulence. Our numerical experiments show that our multiscale model captures the large-scale solution as well as the high order moments very well. In particular, our multiscale model not only captures the correct energy power spectrum, it also reproduces certain important statistical properties that have been observed in experimental studies for fully developed turbulent flows. Moreover, we show that our multiscale method can be used to compute the unknown parameters in a Smagorinsky type of LES model. It is interesting to note that the hybrid LES model which combines an existing LES model with our multiscale method seems to give a better result than the LES model.

The organization of the rest of the paper is as follows. In section 2, we perform multiscale analysis for the 3D Euler equations with multiscale initial data. We also

show how to reparameterize a general multiscale initial condition into a formal two-scale initial condition. Section 3 is devoted to developing the multiscale analysis for the 3D Navier–Stokes equations. In section 4, we will perform some numerical experiments in both two and three space dimensions to confirm our analytical results.

2. Formulation. We consider incompressible 3D Navier–Stokes equations with multiscale solutions:

$$\begin{aligned} &\text{(a)} \quad \partial_t \mathbf{u}^\epsilon + (\mathbf{u}^\epsilon \cdot \nabla)\mathbf{u}^\epsilon + \nabla p^\epsilon = \nu \Delta \mathbf{u}^\epsilon + \mathbf{f}, \\ &\text{(b)} \quad \nabla \cdot \mathbf{u}^\epsilon = 0, \\ &\text{(c)} \quad \mathbf{u}^\epsilon|_{t=0} = \mathbf{U}(\mathbf{x}) + \mathbf{W}\left(\mathbf{x}, \frac{\mathbf{x}}{\epsilon}\right). \end{aligned} \tag{2.1}$$

We remark that the system (2.1) contains infinitely many nonseparated scales, even if it appears in a formal "two-scale" form. We do not consider the boundary effect in our study. The velocity field is assumed to be periodic with period 2π in all directions. In general, the fluid contains infinitely many nonseparable scales. The question of interest is how to derive an averaged equation for the large-scale solution in a systematic way. As a first step, we need to know how to characterize small scales and large scales. The notion of large scales and small scales is relative to a reference scale. From the computation viewpoint, it is more relevant to divide the scales into resolvable scales, which can be accurately resolved by a computational grid, and subgrid scales, which we do not wish to resolve by our computational grid. To capture the large-scale solution accurately, we need to account for or model the effect of subgrid scales. This is the essential difficulty for all turbulent models. In this paper, we will develop a systematic multiscale analysis which allows us to model the subgrid small scales without making any heuristic closure assumption or using unknown parameters.

2.1. Reparameterization of initial data in two-scale structure. In this subsection, we show how to reformulate a general initial condition into a form in which we can apply multiscale analysis. The key idea is to reorganize the scales in the Fourier space into "large scales" and "small scales." As we mentioned before, the large scales are the ones we will resolve by our computational grid, while the small scales are the ones we will capture on the large scales by solving the cell problems.

Let $\mathbf{v}(\mathbf{x})$ be any periodic function on the cubic $[0,1]^3$. By using the Fourier expansion, we can express $\mathbf{v}$ as a Fourier series:

$$\mathbf{v}(\mathbf{x}) = \sum_{\mathbf{k}\in Z^3} \widehat{\mathbf{v}}(\mathbf{k}) \exp\{2\pi i \mathbf{k}\cdot\mathbf{x}\}, \quad i = \sqrt{-1}, \quad \mathbf{k} = (k_1, k_2, k_3), \tag{2.2}$$

where $\widehat{\mathbf{v}}(\mathbf{k})$ are the Fourier coefficients. We choose $0 < \epsilon = 1/E < 1$ to be a reference wavelength, where E is an integer. Let

$$\Lambda_E = \left\{\mathbf{k}; |k_j| \le \frac{E}{2}, \quad 1 \le j \le 3\right\}, \quad \Lambda'_E = Z^3 \backslash \Lambda_E,$$

where $Z^3 = \{\mathbf{k}; k_j \text{ is an integer, } j = 1,2,3\}$. We refer to those Fourier components with $\mathbf{k} \in \Lambda_E$ as large scales, which can be resolved by our computational grid. Similarly, we refer to those Fourier components with $\mathbf{k} \in \Lambda'_E$ as small scales, which need to be captured by solving a cell problem. Based on this consideration, we decompose a function $\mathbf{v}$ into two parts as follows:

$$\mathbf{v} = \mathbf{v}^{(l)}(\mathbf{x}) + \mathbf{v}^{(s)}(\mathbf{x}), \tag{2.3}$$

where

$$\begin{aligned} &\text{(a)}\quad \mathbf{v}^{(l)}(\mathbf{x}) = \sum_{\mathbf{k}\in\Lambda_E} \widehat{\mathbf{v}}(\mathbf{k}) \exp\{2\pi i \mathbf{k}\cdot\mathbf{x}\}, \\ &\text{(b)}\quad \mathbf{v}^{(s)}(\mathbf{x}) = \sum_{\mathbf{k}\in\Lambda'_E} \widehat{\mathbf{v}}(\mathbf{k}) \exp\{2\pi i \mathbf{k}\cdot\mathbf{x}\}. \end{aligned} \tag{2.4}$$

For each $\mathbf{k}$, we rewrite $\mathbf{k}$ as

$$\mathbf{k} = E\mathbf{k}^{(s)} + \mathbf{k}^{(l)}, \tag{2.5}$$

where $\mathbf{k}^{(s)}$ and $\mathbf{k}^{(l)}$ are integers with $\mathbf{k}^{(l)} \in \Lambda_E$. Here the superscripts s and l stand for small-scale and large-scale, respectively. By using (2.5), we have

$$\begin{aligned} \mathbf{v}^{(s)} &= \sum_{\mathbf{k}\in\Lambda'_E} \widehat{\mathbf{v}}(\mathbf{k}) \exp\{2\pi i \mathbf{k}\cdot\mathbf{x}\} \\ &= \sum_{E\mathbf{k}^{(s)}+\mathbf{k}^{(l)}\in\Lambda'_E} \widehat{\mathbf{v}}(E\mathbf{k}^{(s)}+\mathbf{k}^{(l)}) \exp\{2\pi i (E\mathbf{k}^{(s)}+\mathbf{k}^{(l)})\cdot\mathbf{x}\} \\ &= \sum_{\mathbf{k}^{(s)}\neq\mathbf{0}} \left(\sum_{\mathbf{k}^{(l)}\in\Lambda_E} \widehat{\mathbf{v}}(E\mathbf{k}^{(s)}+\mathbf{k}^{(l)}) \exp\{2\pi i \mathbf{k}^{(l)}\cdot\mathbf{x}\} \right) \exp\{2\pi i \mathbf{k}^{(s)}\cdot(E\mathbf{x})\} \\ &= \sum_{\mathbf{k}^{(s)}\neq\mathbf{0}} \widehat{\mathbf{v}}^{(s)}(\mathbf{k}^{(s)},\mathbf{x}) \exp\left\{2\pi i \mathbf{k}^{(s)}\cdot\frac{\mathbf{x}}{\epsilon}\right\} \\ &= \mathbf{v}^{(s)}\left(\mathbf{x},\frac{\mathbf{x}}{\epsilon}\right), \end{aligned} \tag{2.6}$$

where $\epsilon = 1/E$ and

$$\widehat{\mathbf{v}}^{(s)}(\mathbf{k}^{(s)},\mathbf{x}) = \sum_{\mathbf{k}^{(l)}\in\Lambda_E} \widehat{\mathbf{v}}(E\mathbf{k}^{(s)}+\mathbf{k}^{(l)}) \exp\{2\pi i \mathbf{k}^{(l)}\cdot\mathbf{x}\},$$

which contains the Fourier modes with a wave number less than $E/2$. Note that $\mathbf{v}^{(s)}(\mathbf{x},\mathbf{y})$ is a periodic function in $\mathbf{y}$ with mean zero. This provides a constructive proof that we can reformulate any periodic function $\mathbf{v}$ in the following generic form:

$$\mathbf{v}(\mathbf{x}) = \mathbf{v}^{(l)}(\mathbf{x}) + \mathbf{v}^{(s)}\left(\mathbf{x},\frac{\mathbf{x}}{\epsilon}\right), \tag{2.7}$$

where $\mathbf{v}^{(s)}(\mathbf{x},\mathbf{y})$ is a periodic function in $\mathbf{y}$. We can use a coarse grid with size H to resolve low frequency components with wavelength larger than ϵ and a subgrid with size h to resolve high frequency components with wavelength smaller than ϵ.

We would like to emphasize that the above two-scale decomposition is different from the traditional two-scale expansion in the homogenization theory [4]. In the traditional homogenization theory, the functions $\mathbf{v}^{(l)}$ and $\mathbf{v}^{(s)}(\mathbf{x},\mathbf{y})$ are independent of the small-scale parameter ϵ. The question of interest is to study the homogenized solution in the limit as $\epsilon \to 0$. Thus, the homogenization theory relies crucially on the assumption that there is a strong scale separation in the solution. In comparison, we are dealing with solutions which do not have scale separation and contain infinitely many nonseparated scales. A major difference between the two-scale expansion in the homogenization theory and our formal two-scale reparameterization is that the

functions $\mathbf{v}^{(l)}$ and $\mathbf{v}^{(s)}(\mathbf{x},\mathbf{y})$ in our case depend on the small-scale parameter ϵ. If we let $\epsilon \to 0$ as in the homogenization theory, then the large-scale component $\mathbf{v}^{(l)}$ will pick up more and more small-scale components of the solution, and $\mathbf{v}^{(s)}(\mathbf{x},\mathbf{y})$ will tend to zero in the limit. This actually makes sense since ϵ corresponds to the length scale that we would like to resolve by our computational grid. If we let $\epsilon \to 0$, this means that we are willing to resolve more and more small scales in the solution. In the limit, it will become a direct numerical simulation method which attempts to resolve all scales. This is clearly not what we would like to do. In our multiscale model, we will keep ϵ fixed. Its value is determined by the computational grid we will use to resolve the large-scale solution. The challenge for us is to capture the effect of subgrid scales on the resolvable scales by using a systematic multiscale analysis.

3. Multiscale analysis for the 3D Euler equations. We first review some previous results on multiscale analysis for the incompressible Euler equations. Based on the discussion in the previous section, we can formally formulate the multiscale problem for the 3D Euler equations as a homogenization problem with ϵ being a reference wavelength as follows:

$$\begin{aligned} &\text{(a)}\quad \partial_t \mathbf{u}^\epsilon + (\mathbf{u}^\epsilon \cdot \nabla)\mathbf{u}^\epsilon + \nabla p^\epsilon = \mathbf{0}, \\ &\text{(b)}\quad \nabla \cdot \mathbf{u}^\epsilon = 0, \\ &\text{(c)}\quad \mathbf{u}^\epsilon|_{t=0} = \mathbf{U}(\mathbf{x}) + \mathbf{W}\left(\mathbf{x}, \frac{\mathbf{x}}{\epsilon}\right), \end{aligned} \tag{3.1}$$

where $\mathbf{u}^\epsilon(t,\mathbf{x})$ and $p^\epsilon(t,\mathbf{x})$ are the velocity field and the pressure, respectively. We may consider $\mathbf{U}$ as the mean initial velocity field and $\mathbf{W}(\mathbf{x},\mathbf{y})$ as the high frequency component of the initial velocity field. From our construction in the previous subsection, we know that $\mathbf{W}(\mathbf{x},\mathbf{y})$ is periodic in $\mathbf{y}$ with mean zero, i.e.,

$$\langle \mathbf{W} \rangle \equiv \int_{[0,1]^3} \mathbf{W}(\mathbf{x},\mathbf{y}) d\mathbf{y} = \mathbf{0}. \tag{3.2}$$

However, as we show in the previous subsection, ϵ is a reference scale, and the high frequency components $\mathbf{U}$ and $\mathbf{W}(\mathbf{x},\mathbf{y})$ are ϵ-dependent. If we take the limit $\epsilon \to 0$, $\mathbf{W}(\mathbf{x},\mathbf{y})$ will tend to zero, and the mean velocity $\mathbf{U}(\mathbf{x})$ will become the entire velocity field which contains all of the scales. Thus, it is important that one should not keep the function $\mathbf{W}(\mathbf{x},\mathbf{y})$ fixed while taking the limit $\epsilon \to 0$, as one usually does in the homogenization theory.

3.1. MPP model. The homogenization theory of the 3D Euler equations with highly oscillating data was first studied by MPP in 1985 [26]. They adopted a traditional homogenization approach by assuming that the initial velocity field has a two-scale structure as in (3.1)(c). The high frequency component $\mathbf{W}(\mathbf{x},\mathbf{y})$ is assumed to be periodic in $\mathbf{y}$ with mean zero and is independent of ϵ as $\epsilon \to 0$. This assumption implies that there is scale separation in the velocity field. The objective was to derive a homogenized equation that governs the large-scale velocity field as $\epsilon \to 0$. To construct a multiscale expansion for the Euler equations, they made an important assumption that the oscillation is convected by the mean flow. This leads to the following ansatz for the multiscale expansion in the velocity and pressure:

$$\begin{aligned} \mathbf{u}^\epsilon(t,\mathbf{x}) &= \mathbf{u}(t,\mathbf{x}) + \mathbf{w}\left(t,\mathbf{x},\frac{t}{\epsilon},\frac{\boldsymbol{\theta}(t,\mathbf{x})}{\epsilon}\right) + \epsilon \mathbf{u}_1\left(t,\mathbf{x},\frac{t}{\epsilon},\frac{\boldsymbol{\theta}(t,\mathbf{x})}{\epsilon}\right) + \cdots, \\ p^\epsilon(\mathbf{x},t) &= p(t,\mathbf{x}) + q\left(t,\mathbf{x},\frac{t}{\epsilon},\frac{\boldsymbol{\theta}(t,\mathbf{x})}{\epsilon}\right) + \epsilon p_1\left(t,\mathbf{x},\frac{t}{\epsilon},\frac{\boldsymbol{\theta}(t,\mathbf{x})}{\epsilon}\right) + \cdots. \end{aligned}$$

Moreover, $\mathbf{w}(t,\mathbf{x},\tau,\mathbf{y})$, $q(t,\mathbf{x},\tau,\mathbf{y})$, $\mathbf{u}_1(t,\mathbf{x},\tau,\mathbf{y})$, and $p_1(t,\mathbf{x},\tau,\mathbf{y})$ are assumed to be periodic in $\mathbf{y}$ and τ with zero mean. The phase $\boldsymbol{\theta}$ is convected by the mean velocity field $\mathbf{u}$:

$$\frac{\partial \boldsymbol{\theta}}{\partial t} + \mathbf{u}\cdot\nabla\boldsymbol{\theta} = 0, \quad \boldsymbol{\theta}(0,\mathbf{x}) = \mathbf{x}. \tag{3.3}$$

By using multiscale expansion techniques, MPP obtained a periodic cell problem for $\mathbf{w}$ and q. By making additional assumptions on the solution of the cell problem, MPP derived a variant of the $k-\epsilon$ model. We remark that there have been many subsequent contributions in using the homogenization techniques to derive a turbulence model inspired by the pioneering work of MPP [26]; see, e.g., [3, 8, 30, 2, 6, 7, 5].

3.2. A nested multiscale expansion for the 3D Euler equations. In our recent work in [17, 15, 16], we analyzed the structure of the multiscale solution for 2D and 3D Euler equations from a different viewpoint. A key technique is to use a nested multiscale expansion to characterize the propagation of small scales. In order to reveal the multiscale structure of the solution of the 3D Euler equations, we use the vorticity-stream function formulation. Recall that the vorticity is defined as $\boldsymbol{\omega}^\epsilon = \nabla\times\mathbf{u}^\epsilon$, and the velocity field is defined as $\mathbf{u}^\epsilon = \nabla\times\boldsymbol{\psi}^\epsilon$, where the stream function $\boldsymbol{\psi}^\epsilon$ satisfies the following elliptic equation:

$$-\Delta\boldsymbol{\psi}^\epsilon = \boldsymbol{\omega}^\epsilon. \tag{3.4}$$

Define a multiscale phase function $\boldsymbol{\theta}^\epsilon(t,\mathbf{x})$ as follows:

$$\begin{aligned} &\text{(a)}\quad \frac{\partial \boldsymbol{\theta}^\epsilon}{\partial t} + (\mathbf{u}^\epsilon\cdot\nabla)\boldsymbol{\theta}^\epsilon = \mathbf{0},\\ &\text{(b)}\quad \boldsymbol{\theta}^\epsilon|_{t=0} = \mathbf{x}, \end{aligned} \tag{3.5}$$

which is also the inverse flow map. By using this multiscale phase function, we can characterize the evolution of the small-scale vorticity field. In the two-dimensional case, the vorticity is a scalar and is conserved in time. In the three-dimensional case, however, the vorticity is no longer conserved in time due to the presence of vortex stretching in the vorticity equation:

$$\begin{aligned} &\text{(a)}\quad \partial_t\boldsymbol{\omega}^\epsilon + (\mathbf{u}^\epsilon\cdot\nabla)\boldsymbol{\omega}^\epsilon = (\boldsymbol{\omega}^\epsilon\cdot\nabla)\mathbf{u}^\epsilon,\\ &\text{(b)}\quad \boldsymbol{\omega}^\epsilon|_{t=0} = \boldsymbol{\omega}_{int}\left(\mathbf{x},\frac{\mathbf{x}}{\epsilon}\right), \end{aligned} \tag{3.6}$$

where $\boldsymbol{\omega}_{int}$ is the initial vorticity. Note that $\boldsymbol{\theta}^\epsilon$ is the inverse of the flow map. We have a relatively simple expression of vorticity in terms of $\boldsymbol{\theta}^\epsilon$ [9]:

$$\boldsymbol{\omega}^\epsilon(t,\mathbf{x}) = (D\boldsymbol{\theta}^\epsilon)^{-1}\boldsymbol{\omega}_{int}\left(\boldsymbol{\theta}^\epsilon(t,\mathbf{x}),\frac{\boldsymbol{\theta}^\epsilon(t,\mathbf{x})}{\epsilon}\right), \tag{3.7}$$

where $D\boldsymbol{\theta}^\epsilon$ is the Jacobian matrix of $\boldsymbol{\theta}^\epsilon$. Further, we can express the initial vorticity $\boldsymbol{\omega}_{int}$ in terms of the initial velocity field as follows:

$$\boldsymbol{\omega}_{int}(\mathbf{x},\mathbf{y}) = \nabla_x\times\mathbf{U}(\mathbf{x}) + \nabla_x\times\mathbf{W}(\mathbf{x},\mathbf{y}) + \frac{1}{\epsilon}\nabla_y\times\mathbf{W}(\mathbf{x},\mathbf{y}).$$

It is clear from the semianalytic expression (3.7) for vorticity that the small-scale information is propagated along the characteristic variable $\boldsymbol{\theta}^\epsilon$. However, it is not

an easy task to characterize the multiscale structure of $\boldsymbol{\theta}^\epsilon(t,\mathbf{x})$ since its multiscale structure is coupled to that of $\mathbf{u}^\epsilon$. On the other hand, one can see from (3.7) that the small-scale structure in $\boldsymbol{\theta}^\epsilon$ could have an $O(1)$ contribution to the mean velocity field $\mathbf{u}$.

Based on a careful multiscale analysis in the Lagrangian coordinate, which we derive in the appendix, we obtain the following nested multiscale expansion for $\boldsymbol{\theta}^\epsilon$:

$$\boldsymbol{\theta}^\epsilon = \bar{\boldsymbol{\theta}}(t,\mathbf{x},\tau) + \epsilon\widetilde{\boldsymbol{\theta}}(t,\bar{\boldsymbol{\theta}},\tau,\boldsymbol{\theta}^\epsilon/\epsilon), \tag{3.8}$$

where $\tau = t/\epsilon$. The stream function $\boldsymbol{\psi}^\epsilon$ can be expanded similarly. Note that the multiscale structure of $\boldsymbol{\theta}^\epsilon$ is defined implicitly through the fast variable $\mathbf{y} = \boldsymbol{\theta}^\epsilon/\epsilon$. By using this nested multiscale expansion, we can account for many scales which are present in the multiscale solution.

3.3. A change of variables to simplify the computation of the cell problem. The use of the fast variable $\mathbf{y}$ defined above can introduce some difficulty in the numerical implementation. In particular, the elliptic (and the diffusive) part of the cell problem would contain variable coefficients, and these coefficients can undergo severe deformation dynamically. To simplify the computation of the cell problem, we introduce a change of variables from $\mathbf{y}$ to $\mathbf{z}$ as follows:

$$\mathbf{z} = \mathbf{y} - \widetilde{\boldsymbol{\theta}}(t,\bar{\boldsymbol{\theta}},\tau,\mathbf{y}) \equiv \mathcal{G}(\mathbf{y}), \quad \mathbf{y} = \mathcal{G}^{-1}(\mathbf{z}), \tag{3.9}$$

where t, $\bar{\boldsymbol{\theta}}$, and τ are considered as parameters. Let $\widehat{g} = g(\mathbf{y}) = g\circ\mathcal{G}^{-1}(\mathbf{z})$. Note that

$$\mathbf{z}+\mathbf{1} = \mathbf{y}+\mathbf{1} - \widetilde{\boldsymbol{\theta}}(t,\bar{\boldsymbol{\theta}},\tau,\mathbf{y}+\mathbf{1}),$$

where $\mathbf{1} = (1,1,1)^\top$. This implies that $\mathcal{G}^{-1}(\mathbf{z}+\mathbf{1}) = \mathbf{y}+\mathbf{1}$. For each 1-periodic function $g = g(\mathbf{y})$, we have

$$\widehat{g}(\mathbf{z}+\mathbf{1}) = g(\mathbf{y}+\mathbf{1}) = g(\mathbf{y}) = \widehat{g}(\mathbf{z}).$$

Therefore, $\widehat{g}$ is also a 1-periodic function in $\mathbf{z}$. Let us consider the physical meaning of the transformation of (3.9). From (3.8) and (3.9) and the fact that $\mathbf{y} = \boldsymbol{\theta}^\epsilon/\epsilon$, we can easily deduce that $\mathbf{z} = \bar{\boldsymbol{\theta}}/\epsilon$. This implies that $\widetilde{\boldsymbol{\theta}}$ can also be written as

$$\widetilde{\boldsymbol{\theta}} = \widehat{\widetilde{\boldsymbol{\theta}}}\left(t,\bar{\boldsymbol{\theta}},\tau,\frac{\bar{\boldsymbol{\theta}}}{\epsilon}\right). \tag{3.10}$$

To simplify the presentation, we still denote $\widehat{\widetilde{\boldsymbol{\theta}}}$ by $\widetilde{\boldsymbol{\theta}}$. Based upon this observation, we can expand $\boldsymbol{\theta}^\epsilon$ and $\boldsymbol{\psi}^\epsilon$ in the following form:

$$\begin{aligned} &\text{(a)}\quad \boldsymbol{\theta}^\epsilon = \bar{\boldsymbol{\theta}}(t,\mathbf{x},\tau) + \epsilon\widetilde{\boldsymbol{\theta}}(t,\bar{\boldsymbol{\theta}},\tau,\mathbf{z}),\\ &\text{(b)}\quad \boldsymbol{\psi}^\epsilon = \bar{\boldsymbol{\psi}}(t,\mathbf{x},\tau) + \epsilon\widetilde{\boldsymbol{\psi}}(t,\bar{\boldsymbol{\theta}},\tau,\mathbf{z}), \end{aligned} \tag{3.11}$$

where $\mathbf{z}$ and τ are defined as

$$\mathbf{z} = \frac{\bar{\boldsymbol{\theta}}}{\epsilon}, \quad \tau = \frac{t}{\epsilon}, \tag{3.12}$$

respectively, $\bar{\boldsymbol{\theta}}$ and $\bar{\boldsymbol{\psi}}$ are averages of $\boldsymbol{\theta}^\epsilon$ and $\boldsymbol{\psi}^\epsilon$, respectively, with respect to $\mathbf{z}$ over one period, and $\widetilde{\boldsymbol{\theta}}$ and $\widetilde{\boldsymbol{\psi}}$ are 1-periodic functions in $\mathbf{z}$ with zero mean. Now direct calculations give

$$\mathbf{u}^\epsilon = \nabla_x\times\bar{\boldsymbol{\psi}} + (D_x\bar{\boldsymbol{\theta}}^\top\nabla_z)\times\widetilde{\boldsymbol{\psi}} + \epsilon\nabla_x\times\widetilde{\boldsymbol{\psi}}, \tag{3.13}$$

which implies that the velocity has the following multiscale expansion:

$$\mathbf{u}^\epsilon = \bar{\mathbf{u}}(t,\mathbf{x},\tau) + \widetilde{\mathbf{u}}(t,\bar{\boldsymbol{\theta}},\tau,\mathbf{z}), \tag{3.14}$$

where $\widetilde{\mathbf{u}}$ is periodic in $\mathbf{z}$ and has zero mean. Note that $\bar{\mathbf{u}}$ is the total mean velocity field which contains higher order terms in the expansion.

4. Multiscale analysis of Navier–Stokes equations. Based on the understanding we gain from the multiscale analysis for the Euler equations, we are now ready to perform multiscale analysis for the Navier–Stokes equations. Motivated by the analysis from the previous section, we perform multiscale expansion for $(\mathbf{u}^\epsilon, p^\epsilon)$ in the form:

$$\begin{aligned} &\text{(a)}\quad \mathbf{u}^\epsilon = \bar{\mathbf{u}}(t,\mathbf{x},\tau) + \widetilde{\mathbf{u}}(t,\bar{\boldsymbol{\theta}},\tau,\mathbf{z}),\\ &\text{(b)}\quad p^\epsilon = \bar{p}(t,\mathbf{x},\tau) + \widetilde{p}(t,\bar{\boldsymbol{\theta}},\tau,\mathbf{z}), \end{aligned} \tag{4.1}$$

where $\mathbf{z} = \frac{\bar{\boldsymbol{\theta}}}{\epsilon}$, $\tau = \frac{t}{\epsilon}$, $(\bar{\mathbf{u}}, \bar{p})$ and $\bar{\boldsymbol{\theta}}$ are total mean components including higher order terms, and $\widetilde{\mathbf{u}}$ and $\widetilde{p}$ are periodic in $\mathbf{z}$ with zero mean.

4.1. Averaged equations. In this subsection, we derive the averaged equations for $\bar{\mathbf{u}}$ and $\bar{\boldsymbol{\theta}}$. Let us denote by $\bar{\partial}_t = \partial_t + \epsilon^{-1}\partial_\tau$ the total derivative in time. By substituting the expansion (4.1) into the Navier–Stokes equations, we get

$$\begin{aligned} &\bar{\partial}_t\bar{\mathbf{u}} + \left(\partial_t + \frac{1}{\epsilon}\partial_\tau\right)\widetilde{\mathbf{u}} + \frac{1}{\epsilon}D_z\widetilde{\mathbf{u}}\bar{\partial}_t\bar{\boldsymbol{\theta}} + \left(\nabla_x + \frac{1}{\epsilon}D_x\bar{\boldsymbol{\theta}}^\top\nabla_z\right)\cdot((\bar{\mathbf{u}}+\widetilde{\mathbf{u}})\otimes(\bar{\mathbf{u}}+\widetilde{\mathbf{u}}))\\ &\quad + \nabla_x\bar{p} + \left(\nabla_x + \frac{1}{\epsilon}D_x\bar{\boldsymbol{\theta}}^\top\nabla_z\right)\widetilde{p} - \nu\left(\Delta_x + \frac{1}{\epsilon}\nabla_x\cdot(D_x\bar{\boldsymbol{\theta}}^\top\nabla_z)\right.\\ &\quad \left. + \frac{1}{\epsilon}\nabla_z\cdot(D_x\bar{\boldsymbol{\theta}}\nabla_x) + \frac{1}{\epsilon^2}\nabla_z\cdot(D_x\bar{\boldsymbol{\theta}}D_x\bar{\boldsymbol{\theta}}^\top\nabla_z)\right)(\bar{\mathbf{u}}+\widetilde{\mathbf{u}}) = \mathbf{f}, \end{aligned} \tag{4.2}$$

and

$$\left(\nabla_x + \frac{1}{\epsilon}D_x\bar{\boldsymbol{\theta}}^\top\nabla_z\right)\cdot(\bar{\mathbf{u}}+\widetilde{\mathbf{u}}) = 0, \tag{4.3}$$

where $\mathbf{u}\otimes\mathbf{u}$ is defined as a 3×3 symmetric matrix whose (i,j)th entry is given by u_ju_i, $\mathbf{u} = (u_1,u_2,u_3)$, $i,j = 1,2,3$. By averaging (4.2) with respect to $\mathbf{z}$, we get

$$\bar{\partial}_t\bar{\mathbf{u}} + \nabla_x\cdot(\bar{\mathbf{u}}\otimes\bar{\mathbf{u}}) + \nabla_x\cdot\langle\widetilde{\mathbf{u}}\otimes\widetilde{\mathbf{u}}\rangle + \nabla_x\bar{p} = \nu\Delta\bar{\mathbf{u}} + \mathbf{f}. \tag{4.4}$$

By averaging (3.13) with respect to $\mathbf{z}$, we obtain $\bar{\mathbf{u}} = \nabla_x\times\bar{\boldsymbol{\psi}}$, which implies that

$$\nabla_x\cdot\bar{\mathbf{u}} = 0. \tag{4.5}$$

Next, we substitute the expansion (3.11) into (3.5), and we obtain

$$\bar{\partial}_t\bar{\boldsymbol{\theta}} + \partial_\tau\widetilde{\boldsymbol{\theta}} + D_z\widetilde{\boldsymbol{\theta}}\bar{\partial}_t\bar{\boldsymbol{\theta}} + \epsilon\partial_t\widetilde{\boldsymbol{\theta}} + \left(\nabla_x + \frac{1}{\epsilon}D_x\bar{\boldsymbol{\theta}}^\top\nabla_z\right)\cdot((\bar{\boldsymbol{\theta}}+\epsilon\widetilde{\boldsymbol{\theta}})\otimes(\bar{\mathbf{u}}+\widetilde{\mathbf{u}})) = \mathbf{0}. \tag{4.6}$$

By averaging (4.6) with respect to $\mathbf{z}$, we get

$$\bar{\partial}_t\bar{\boldsymbol{\theta}} + \nabla_x\cdot(\bar{\boldsymbol{\theta}}\otimes\bar{\mathbf{u}}) + \epsilon\nabla_x\cdot\langle\widetilde{\boldsymbol{\theta}}\otimes\widetilde{\mathbf{u}}\rangle = \mathbf{0}. \tag{4.7}$$

The additional term $\langle \widetilde{\mathbf{u}} \otimes \widetilde{\mathbf{u}} \rangle$ in the averaged equations (4.4) is called the Reynolds stress. How to model the Reynolds stress is important in both theoretical understanding and engineering applications. In many LES models, the Reynolds stress is modeled by making some closure assumption with unknown parameters to be determined from experimental data. In comparison, our multiscale analysis gives a self-consistent system which couples the large-scale dynamics to the subgrid-scale dynamics in a natural way without unknown parameters. To simplify our multiscale model further, we will study the leading order terms of $(\widetilde{\mathbf{u}}, \widetilde{p})$. To this end, we expand $(\widetilde{\mathbf{u}}, \widetilde{p})$ and $\widetilde{\boldsymbol{\theta}}$ in the form:

$$\begin{aligned} &\text{(a)} \quad \widetilde{\mathbf{u}} = \mathbf{w}(t, \bar{\boldsymbol{\theta}}, \tau, \mathbf{z}) + O(\epsilon), \\ &\text{(b)} \quad \widetilde{p} = q(t, \bar{\boldsymbol{\theta}}, \tau, \mathbf{z}) + O(\epsilon), \\ &\text{(c)} \quad \widetilde{\boldsymbol{\theta}} = \boldsymbol{\Theta}(t, \bar{\boldsymbol{\theta}}, \tau, \mathbf{z}) + O(\epsilon). \end{aligned} \tag{4.8}$$

It follows from (4.3) and (4.5) that

$$(\epsilon \nabla_x + D_x \bar{\boldsymbol{\theta}}^\top \nabla_z) \cdot \widetilde{\mathbf{u}} = 0,$$

which implies that

$$D_x \bar{\boldsymbol{\theta}}^\top \nabla_z \cdot \mathbf{w} = 0. \tag{4.9}$$

It follows from (4.2) and (4.4) that

$$\begin{aligned} &\frac{1}{\epsilon}\Big(\partial_\tau \widetilde{\mathbf{u}} + D_z \widetilde{\mathbf{u}} \bar{\partial}_t \bar{\boldsymbol{\theta}} + (D_x \bar{\boldsymbol{\theta}}^\top \nabla_z) \cdot (\bar{\mathbf{u}} \otimes \widetilde{\mathbf{u}}) + (\widetilde{\mathbf{u}} \otimes \bar{\mathbf{u}} + \widetilde{\mathbf{u}} \otimes \widetilde{\mathbf{u}}) + D_x \bar{\boldsymbol{\theta}}^\top \nabla_z \widetilde{p}\Big) \\ &\quad - \frac{\nu}{\epsilon^2} \nabla_z \cdot (D_x \bar{\boldsymbol{\theta}} D_x \bar{\boldsymbol{\theta}}^\top \nabla_z \widetilde{\mathbf{u}}) \\ &\quad + \partial_t \widetilde{\mathbf{u}} + \nabla_x \cdot (\bar{\mathbf{u}} \otimes \widetilde{\mathbf{u}} + \widetilde{\mathbf{u}} \otimes (\bar{\mathbf{u}} + \widetilde{\mathbf{u}})) - \nabla_x \cdot \langle \widetilde{\mathbf{u}} \otimes \widetilde{\mathbf{u}} \rangle \\ &\quad + \nabla_x \widetilde{p} - \frac{\nu}{\epsilon}(\nabla_x \cdot (D_x \bar{\boldsymbol{\theta}}^\top \nabla_z \widetilde{\mathbf{u}}) + \nabla_z \cdot (D_x \bar{\boldsymbol{\theta}} \nabla_x \widetilde{\mathbf{u}})) = \mathbf{0}. \end{aligned} \tag{4.10}$$

Note that

$$\begin{aligned} &\frac{1}{\epsilon}[(D_x \bar{\boldsymbol{\theta}}^\top \nabla_z) \cdot (\bar{\mathbf{u}} \otimes \widetilde{\mathbf{u}} + \widetilde{\mathbf{u}} \otimes \bar{\mathbf{u}} + \widetilde{\mathbf{u}} \otimes \widetilde{\mathbf{u}}) \,] \\ &\qquad + \nabla_x \cdot (\bar{\mathbf{u}} \otimes \widetilde{\mathbf{u}} + \widetilde{\mathbf{u}} \otimes (\bar{\mathbf{u}} + \widetilde{\mathbf{u}})) \\ &\quad = \frac{1}{\epsilon}[D_z \widetilde{\mathbf{u}} D_x \bar{\boldsymbol{\theta}} (\bar{\mathbf{u}} + \widetilde{\mathbf{u}}) + (\bar{\mathbf{u}} + \widetilde{\mathbf{u}})(D_x \bar{\boldsymbol{\theta}}^\top \nabla_z) \cdot \widetilde{\mathbf{u}} \,] \\ &\qquad + (\bar{\mathbf{u}} \cdot \nabla_x) \widetilde{\mathbf{u}} + (\widetilde{\mathbf{u}} \cdot \nabla_x) \bar{\mathbf{u}} + (\widetilde{\mathbf{u}} \cdot \nabla_x) \widetilde{\mathbf{u}} + (\bar{\mathbf{u}} + \widetilde{\mathbf{u}}) \nabla_x \cdot \widetilde{\mathbf{u}} \\ &\quad = \frac{1}{\epsilon} D_z \widetilde{\mathbf{u}} D_x \bar{\boldsymbol{\theta}} (\bar{\mathbf{u}} + \widetilde{\mathbf{u}}) + (\bar{\mathbf{u}} \cdot \nabla_x) \widetilde{\mathbf{u}} + (\widetilde{\mathbf{u}} \cdot \nabla_x) \bar{\mathbf{u}} + (\widetilde{\mathbf{u}} \cdot \nabla_x) \widetilde{\mathbf{u}}. \end{aligned}$$

By using the above equation and multiplying (4.10) by ϵ, we obtain

$$\begin{aligned} &\partial_\tau \widetilde{\mathbf{u}} + D_z \widetilde{\mathbf{u}} D_x \bar{\boldsymbol{\theta}} \widetilde{\mathbf{u}} + D_x \bar{\boldsymbol{\theta}}^\top \nabla_z \widetilde{p} = \frac{\nu}{\epsilon}\Big(\nabla_z \cdot (D_x \bar{\boldsymbol{\theta}} D_x \bar{\boldsymbol{\theta}}^\top \nabla_z \widetilde{\mathbf{u}}) \\ &+ \epsilon(\nabla_x \cdot (D_x \bar{\boldsymbol{\theta}}^\top \nabla_z \widetilde{\mathbf{u}}) + \nabla_z \cdot (D_x \bar{\boldsymbol{\theta}} \nabla_x \widetilde{\mathbf{u}}))\Big) + O(\epsilon). \end{aligned}$$

To the leading order approximation, we neglect the $O(\epsilon)$ terms associated with the diffusion operator. This gives

$$\partial_\tau \mathbf{w} + D_z \mathbf{w} D_x \bar{\boldsymbol{\theta}} \mathbf{w} + D_x \bar{\boldsymbol{\theta}}^\top \nabla_z q = \frac{\nu}{\epsilon} \nabla_z \cdot (D_x \bar{\boldsymbol{\theta}} D_x \bar{\boldsymbol{\theta}}^\top \nabla_z \mathbf{w}). \tag{4.11}$$

Note that $\frac{\nu}{\epsilon}$ corresponds to the cell viscosity coefficient. It follows from (4.6) that

$$\partial_\tau \widetilde{\boldsymbol{\theta}} + D_z \widetilde{\boldsymbol{\theta}} D_x \bar{\boldsymbol{\theta}} \widetilde{\mathbf{u}} + D_x \bar{\boldsymbol{\theta}} \widetilde{\mathbf{u}} = 0. \tag{4.12}$$

This implies that

$$\partial_\tau \boldsymbol{\Theta} + (\mathcal{I} + D_z \boldsymbol{\Theta}) D_x \bar{\boldsymbol{\theta}} \mathbf{w} = 0. \tag{4.13}$$

Thus we obtain the following multiscale model which governs the leading velocity field and the subgrid velocity field:

Multiscale model I.

(1) Averaged equations for the leading order velocity:

$$\begin{aligned} &\text{(a)}\ \ \bar{\partial}_t \bar{\mathbf{u}} + (\bar{\mathbf{u}} \cdot \nabla_x)\bar{\mathbf{u}} + \nabla_x \bar{p} + \nabla_x \cdot \langle \mathbf{w} \otimes \mathbf{w} \rangle = \nu \Delta \bar{\mathbf{u}} + \mathbf{f}, \\ &\text{(b)}\ \ \nabla_x \cdot \bar{\mathbf{u}} = 0, \\ &\text{(c)}\ \ \bar{\mathbf{u}}|_{t=0} = \mathbf{U}(\mathbf{x}), \end{aligned} \tag{4.14}$$

where f is a coarse scale forcing.

(2) Averaged equations for the leading order Lagrangian map:

$$\begin{aligned} &\text{(a)}\ \ \bar{\partial}_t \bar{\boldsymbol{\theta}} + (\bar{\mathbf{u}} \cdot \nabla_x)\bar{\boldsymbol{\theta}} + \epsilon \nabla_x \cdot \langle \boldsymbol{\Theta} \otimes \mathbf{w} \rangle = \mathbf{0}, \\ &\text{(b)}\ \ \bar{\boldsymbol{\theta}}|_{t=0} = \mathbf{x}. \end{aligned} \tag{4.15}$$

(3) Leading order equations for the fluctuation of the velocity:

$$\begin{aligned} &\text{(a)}\ \ \partial_\tau \mathbf{w} + D_z \mathbf{w} D_x \bar{\boldsymbol{\theta}} \mathbf{w} + D_x \bar{\boldsymbol{\theta}}^\top \nabla_z q = \frac{\nu}{\epsilon} \nabla_z \cdot (D_x \bar{\boldsymbol{\theta}} D_x \bar{\boldsymbol{\theta}}^\top \nabla_z \mathbf{w}); \\ &\text{(b)}\ \ \left(D_x \bar{\boldsymbol{\theta}}^\top \nabla_z \right) \cdot \mathbf{w} = 0, \\ &\text{(c)}\ \ \mathbf{w}|_{\tau = t = 0} = \mathbf{W}(\mathbf{x}, \mathbf{z}). \end{aligned} \tag{4.16}$$

(5) Leading order equations for the fluctuation of the Lagrangian map:

$$\begin{aligned} &\text{(a)}\ \ \partial_\tau \boldsymbol{\Theta} + (\mathcal{I} + D_z \boldsymbol{\Theta}) D_x \bar{\boldsymbol{\theta}} \mathbf{w} = \mathbf{0}. \\ &\text{(b)}\ \ \boldsymbol{\Theta}|_{\tau = t = 0} = \mathbf{0}. \end{aligned} \tag{4.17}$$

The above multiscale model provides a systematic multiscale model for the Reynolds stress. An important feature of our multiscale model is that there is no closure assumption and there are no unknown parameters to be determined. It is a self-consistent multiscale model which captures the dynamic interaction between the large-scale solution and the small-scale solution. In the next subsection, we will discuss some numerical implementation issues in discretizing the above multiscale model.

4.2. Numerical implementation. In this subsection, we will give a computational algorithm to compute the averaged equations. Take Δt as the time step for the averaged solution. For $m \geq 0$, let $t_m = m\Delta t$ and $\tau_m = m\Delta t/\epsilon$. Let $\Delta = \Delta t/\epsilon$, and define $[f]^*$ to be the local time average given by

$$[f^m]^*_\Delta = \frac{1}{\Delta} \int_{\tau_{m-1}}^{\tau_m} f d\tau. \tag{4.18}$$

Note that $\bar{\mathbf{u}}$ still depends on the fast time scale τ. In order to derive a multiscale model for the large-scale solution which is independent of the fast time scale, we

perform a local time average to eliminate the dependence of the mean velocity field on the fast time scale. Observe that the large-scale solution $\bar{\mathbf{u}}$ has the form

$$\bar{\mathbf{u}}(t,\mathbf{x},\tau) = \mathbf{u}(t,\mathbf{x}) + \epsilon \mathbf{u}_1(t,\mathbf{x},\tau).$$

By integrating the cell problem (4.16) in τ from τ_{m-1} to τ_m while keeping $\mathbf{x}$ and t fixed as parameters, we obtain the following one-step explicit computational algorithm.

ALGORITHM. For $m \geq 0$, let $t_m = m\Delta t$ and $\tau_m = m\Delta t/\epsilon$.

Step 1. At $t = 0$ and $\tau = 0$, we set

$$\boldsymbol{\theta}_{int} = \mathbf{x}, \quad \mathbf{u}_{int} = \mathbf{U}, \quad \mathbf{w}_{int} = \mathbf{W}, \quad \boldsymbol{\Theta}_{int} = \mathbf{0}, \quad \mathcal{A} = \mathcal{I}. \tag{4.19}$$

Then start the iteration for $m = 0, 1, \ldots$ as follows:

Step 2 (update the small-scale solution). Solve for $(\mathbf{w}, q)$ from the following system for $\tau_m < \tau \leq \tau_{m+1}$ with a subgrid time step size $\Delta\tau$ while keeping $\mathbf{x}$ and t fixed as parameters:

$$\begin{aligned} &\text{(a)} \quad \partial_\tau \mathbf{w} + D_z \mathbf{w} \mathcal{A}\mathbf{w} + \mathcal{A}^\top \nabla_z q - \frac{\nu}{\epsilon} \nabla \cdot (\mathcal{A}\mathcal{A}^\top \nabla_z \mathbf{w}) = \mathbf{0}; \\ &\text{(b)} \quad \left(\mathcal{A}^\top \nabla_z\right) \cdot \mathbf{w} = 0, \\ &\text{(c)} \quad \mathbf{w}|_{\tau=\tau_m} = \mathbf{w}_{int} \end{aligned} \tag{4.20}$$

and

$$\begin{aligned} &\text{(a)} \quad \partial_\tau \boldsymbol{\Theta} + (\mathcal{I} + D_z \boldsymbol{\Theta}) D_x \bar{\boldsymbol{\theta}} \mathbf{w} = \mathbf{0}. \\ &\text{(b)} \quad \boldsymbol{\Theta}|_{\tau=t=0} = \boldsymbol{\Theta}_{int}. \end{aligned} \tag{4.21}$$

Step 3 (update the large-scale solution). Solve for $(\mathbf{u}, p)$ and $\boldsymbol{\theta}$ from the following system for $t_m \leq t \leq t_{m+1}$:

$$\begin{aligned} &\text{(a)} \quad \partial_t \mathbf{u} + (\mathbf{u} \cdot \nabla_x)\mathbf{u} + \nabla_x p + \nabla_x \cdot \langle [\mathbf{w} \otimes \mathbf{w}]^*_\Delta \rangle - \nu \Delta \mathbf{u} = \mathbf{f}, \\ &\text{(b)} \quad \nabla_x \cdot \mathbf{u} = 0, \\ &\text{(c)} \quad \mathbf{u}|_{t=t_m} = \mathbf{u}_{int}, \end{aligned} \tag{4.22}$$

and

$$\begin{aligned} &\text{(a)} \quad \partial_t \boldsymbol{\theta} + (\mathbf{u} \cdot \nabla_x)\boldsymbol{\theta} + \epsilon \nabla_x \cdot \langle [\boldsymbol{\Theta} \otimes \mathbf{w}]^*_\Delta \rangle = \mathbf{0}, \\ &\text{(b)} \quad \boldsymbol{\theta}|_{t=t_m} = \boldsymbol{\theta}_{int}. \end{aligned} \tag{4.23}$$

Step 4 (restart the next time step). Let

$$\begin{aligned} &\boldsymbol{\theta}_{int} = \boldsymbol{\theta}|_{t=t_{m+1}}, \quad \mathbf{u}_{int} = \mathbf{u}|_{t=t_{m+1}}, \quad \mathbf{w}_{int} = \mathbf{w}|_{\tau=\tau_{m+1}}, \\ &\boldsymbol{\Theta}_{int} = \boldsymbol{\Theta}|_{\tau=\tau_{m+1}}, \quad \mathcal{A} = D_x \boldsymbol{\theta}|_{t=t_{m+1}}. \end{aligned} \tag{4.24}$$

Return to step 2 to restart the next time step.

Remark 4.1. Note that we have neglected the $O(\epsilon)$ term in the $\boldsymbol{\theta}$ equation. The above one-step algorithm can be easily generalized to a high order algorithm.

Remark 4.2. In our numerical implementation, the cell problem (4.20) can be further simplified by making the following change of variables from $\mathbf{w}$ to $\tilde{\mathbf{w}}$ by letting $\tilde{\mathbf{w}} = \mathcal{A}\mathbf{w}$. Then $\tilde{\mathbf{w}}$ satisfies the following modified cell problem:

$$\begin{aligned} &\text{(a)} \quad \partial_\tau \tilde{\mathbf{w}} + \tilde{\mathbf{w}} \cdot \nabla_z \tilde{\mathbf{w}} + \mathcal{A}\mathcal{A}^\top \nabla_z q - \frac{\nu}{\epsilon} \nabla \cdot (\mathcal{A}\mathcal{A}^\top \nabla_z \tilde{\mathbf{w}}) = \mathbf{0}; \\ &\text{(b)} \quad \nabla_z \cdot \tilde{\mathbf{w}} = 0, \\ &\text{(c)} \quad \tilde{\mathbf{w}}|_{\tau=\tau_m} = \mathcal{A}\mathbf{w}_{int}. \end{aligned} \tag{4.25}$$

The above modified cell problem can be solved more easily.

5. Numerical experiments. In the previous section, we performed a systematic multiscale analysis for the incompressible Navier–Stokes equations and proposed a new multiscale model which captures the dynamic interplay between the large-scale solution and the small-scale cell problem. In this section, we will perform detailed numerical experiments in both two and three space dimensions to demonstrate the accuracy of our multiscale model.

5.1. Numerical experiments for the 2D Navier–Stokes equations. We first perform numerical experiments in two space dimensions. Specifically, we solve the 2D incompressible Navier–Stokes equations in a doubly periodic box of size $2\pi\times 2\pi$. For the multiscale problem, we solve the averaged equations given in section 3 but with a simplified cell problem for $\mathbf{w}$ by ignoring the cell viscosity term. In this case, we can solve for the cell problem by using the stream function vorticity formulation; see section 4.1 of [15].

A pseudospectral method is used to solve both the averaged equations and the subgrid cell problem. We use the second order Runge–Kutta method to discretize the equation in time. In our computations, we solve the averaged equation by using a coarse grid and large time step Δt. For each coarse grid point within the time interval from t_n to t_{n+1}, with $t_n = n\Delta t$, we solve the cell problem with the periodic boundary condition in the $\mathbf{z}$ variable from $\tau_n = t_n/\epsilon$ to $\tau_{n+1} = t_{n+1}/\epsilon$ by using a subgrid $\Delta\mathbf{z}$ and a subgrid time step $\Delta\tau$. Note that each cell problem is decoupled from the others. We then average the cell solution from τ_n to τ_{n+1} to evaluate the Reynolds stress term and update the mean velocity at t_{n+1}. To eliminate the aliasing error in the pseudospectral method, we use a 15th order Fourier smoothing function to damp the high frequency modes. Specifically, the Fourier smoothing function we use is given by $\rho(k_i) = \exp(-10(k_i/N)^{15})$ for $|k_i| \le N$, $k = (k_1, k_2)$ is the wave number in the Fourier transform, and $2N$ is the number of Fourier modes in each dimension. This smoothing function is multiplied to the kth Fourier coefficient of a physical variable in each dimension.

Below we present some numerical results on the decay of 2D homogeneous turbulence and compare our multiscale model with the well-resolved direct numerical simulation (DNS). The DNS uses a 512×512 fine grid. The simulation starts with a random initial condition, where the initial distribution of the stream function in the Fourier space is given by

$$|\hat{\psi}(k)| = \frac{k}{k^4 + \delta}, \quad k = |\mathbf{k}|, \tag{5.1}$$

with random phases. This choice of initial velocity field is similar to the earlier work of Henshaw, Kreiss, and Reyna [13] (see also [10]). In the computation, we choose $\delta = 10^{-5}$. The initial vorticity distribution is plotted in Figure 5.1. We choose $\nu = 10^{-4}$ in our computations. The corresponding Reynolds number based on the initial rms (root mean square) velocity is about 31,000. At $t = 5.0$, coherent vortices emerge from the random initial condition, which is denoted as the "vortex generation period." At later stages, the flow is dominated by the mutual interactions of coherent vortices. The number of vortices decreases, and the averaged vortex radius and circulation increase.

Since our multiscale analysis is developed for well-mixed flows, we start the multiscale computation by using our multiscale model starting at $t = 5.0$ when the flow completes the vortex generation period. We use the technique presented in section 2.1 to prepare the velocity obtained from the DNS at $t = 5.0$ in the form of a two-scale

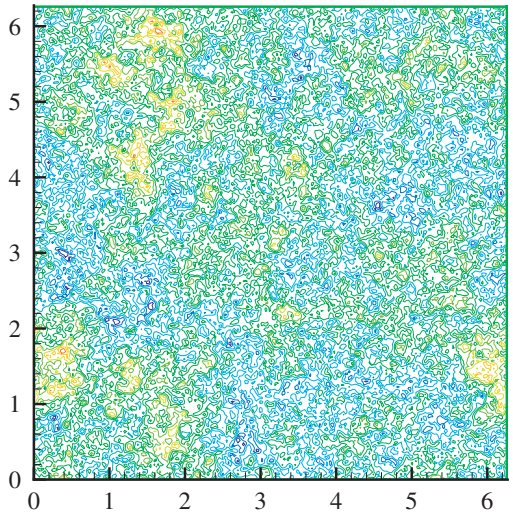

FIG. 5.1. *Vorticity contour at* $t = 0$.

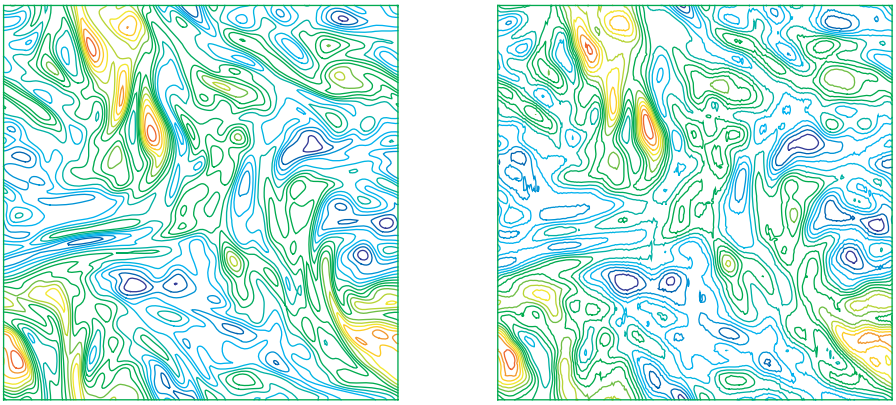

FIG. 5.2. *Vorticity contours at* $t = 5$. *The picture on the left is obtained by DNS, and the picture on the right is obtained by our multiscale method.*

initial condition so that we can apply our multiscale model to solve the multiscale problem. The dimension of the coarse grid (slow variables) is 64×64, and that of the small scale (fast variables) is 32×32. This gives $\epsilon = 1/64$. The time step for the multiscale model is $\Delta t = 0.01$, and the subgrid time step for the cell problem is $\Delta\tau = 0.01$. Figures 5.2–5.4 compare the vorticity distribution of the multiscale model with the DNS result at $t = 5.0$, 10.0, and 20.0, respectively. We reconstruct the fine grid vorticity by adding the mean vorticity field to the subgrid vorticity field; see (5.2). The plots show that there is a strong shearing and stretching of the vorticity contours by the mean flow. In addition, the size of the vortices grows due to the merger of vorticity of the same sign, which is one of the mechanisms that contributes to the inverse energy cascade. The vorticity distribution from the multiscale model is in excellent agreement with the DNS, suggesting that the multiscale model captures the vortex interactions at both large scales and small scales.

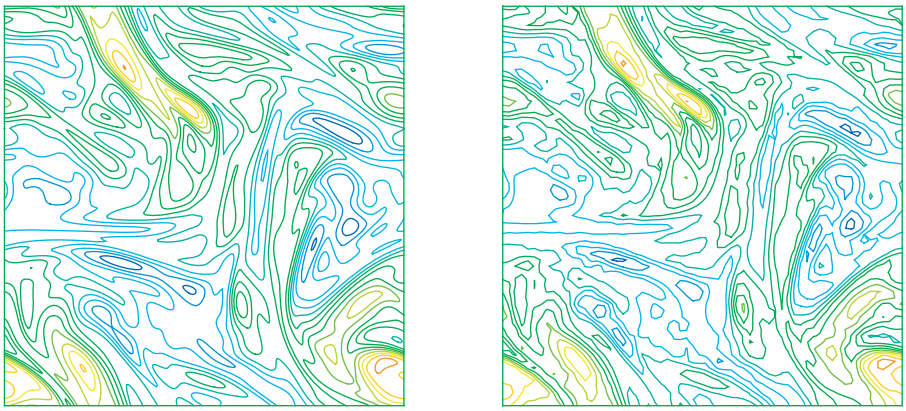

FIG. 5.3. *Vorticity contours at $t = 10$. The picture on the left is obtained by DNS, and the picture on the right is obtained by our multiscale method.*

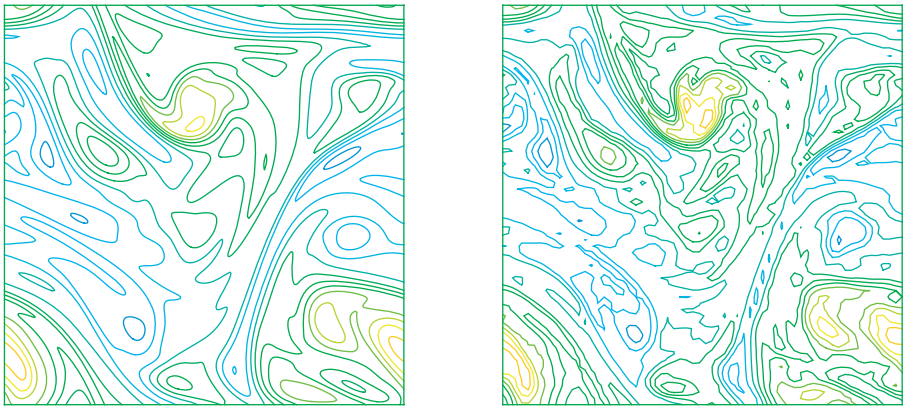

FIG. 5.4. *Vorticity contours at $t = 20$. The picture on the left is obtained by DNS, and the picture on the right is obtained by our multiscale method.*

The accuracy of the solution can be examined by studying whether the solution dissipates the correct amount of energy and enstrophy, which are two statistical global quantities of turbulent flows. For a high Reynolds number flow, the kinetic energy does not change much dynamically. On the other hand, there exists a cascade of enstrophy from large scales to small scales [1, 23], which causes the total enstrophy to decay in time. Specifically, vorticity gradients are amplified with the formation of thin filaments. These fine structures evolve until they reach the very small dissipation scales, so that the enstrophy and all positive-order vorticity moments decay. In Figure 5.5, we show the temporal evolution of the total kinetic energy and the total enstrophy by using three different approaches, which are (i) the DNS, (ii) the simulation using our multiscale model, and (iii) the simulation of the multiscale model ignoring the Reynolds stress term. With very small viscosity, the energy decay from all 3 simulations is negligible. On the other hand, enstrophy decays continuously, with the maximum decay rate occurring during the initial vortex formation period for $t \leq 5$. The decay rate becomes smaller during the vortex merger stage which takes place after $t = 5$. We can see that the simulation with a coarse grid using

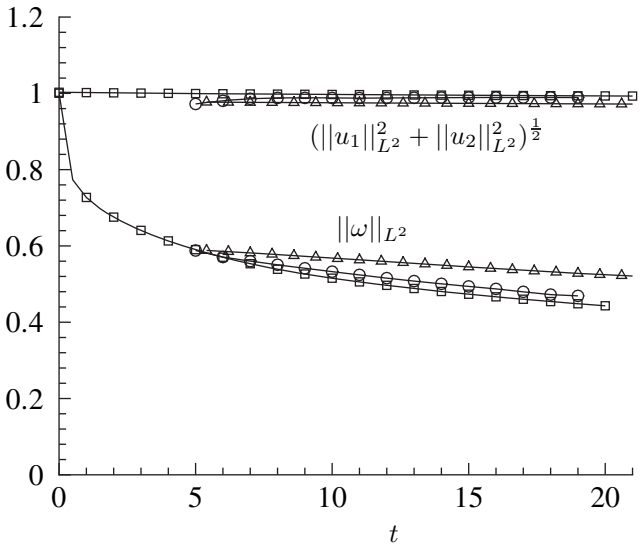

FIG. 5.5. *Temporal evolution of kinetic energy* $(||u_1||^2_{L^2} + ||u_2||^2_{L^2})^{\frac{1}{2}}$ *and enstrophy* $||\omega||_{L^2}$. *(□), DNS (*$N = 512$*); (○), multiscale model; (△), without Reynolds stress terms.*

approach (iii) leads to much slower enstrophy decay because it could not capture the enstrophy cascade from large scales to the dissipation scale. On the other hand, the enstrophy decay rate of the simulation using our multiscale model is very close to that of the DNS, suggesting that the dissipation mechanism is well resolved within each cell.

We also compare the spectra obtained by the DNS with those obtained by solving our multiscale model at $t = 20.0$. We reconstruct the fine grid velocity field by using the leading order approximation

$$\mathbf{u}^{\epsilon}(t, \mathbf{x}) \approx \mathbf{u}(t, \mathbf{x}) + \mathbf{w}\left(t, \boldsymbol{\theta}, \tau, \frac{\boldsymbol{\theta}(\mathbf{t}, \mathbf{x})}{\epsilon}\right), \tag{5.2}$$

where the fine grid phase function is obtained by using the spectral interpolation. The result is shown in Figure 5.6. The agreement is very good at low wave numbers. At high wave numbers, the DNS spectra decay faster than the spectra of the simulation using the multiscale model. This explains the difference in the enstrophy decay rate between the two simulations. The difference is partly due to neglecting the higher order terms in our multiscale model and the cell problem. Another more important reason is that there is viscous dissipation in all of the scales in the DNS, whereas we neglect viscosity in the cell problem in the multiscale model. Nonetheless, our multiscale model accurately captures the dynamics of the large scale as well as the averaged effect from the small scales.

5.2. Numerical experiments for the 3D Navier–Stokes equations. In this subsection, we perform a careful DNS of the 3D Navier–Stokes equations to check the accuracy of the multiscale analysis presented in the previous sections. Given the number of grid points and the size of the computational domain, the smallest resolved length scale or, equivalently, the largest wave number k_{max} is prescribed. In a three-dimensional turbulent flow, the kinetic energy cascades in time to smaller,

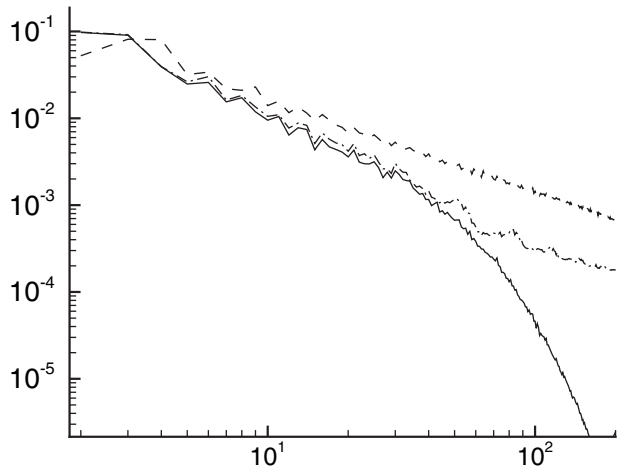

FIG. 5.6. *Spectrum of velocity component* u_1. *(Dashed line),* $t = 0.0$*; (solid line), DNS,* $t = 20.0$*; (dashed-dotted line), multiscale model,* $t = 20.0$.

more dissipative scales. The scale at which the viscous dissipation becomes dominant, and which represents the smallest scales of turbulence, is characterized by the Kolmogorov length scale η. In a fully resolved DNS, the condition $k_{max}\eta < 1$ is necessary for the small scales to be adequately represented. Consequently, k_{max} limits the highest achievable Reynolds number in a direct numerical simulation for a given computational box.

There are three main characteristic length scales in an isotropic turbulent flow: the integral scale I characterizing the energy containing scales is defined as

$$I = \frac{3\pi}{4} \frac{\int_0^{k_{max}} \frac{E(k)}{k} dk}{\int_0^{k_{max}} E(k) dk}, \tag{5.3}$$

where $E(k)$ is the energy spectrum function at the scalar wave number k; the Kolmogorov microscale η representative of dissipative scale is

$$\eta = \left(\frac{\nu^3}{\epsilon}\right)^{1/4}, \tag{5.4}$$

where ϵ is the volume averaged energy-dissipation rate; and the Taylor microscale λ characterizing the mixed energy dissipation scales is defined as [11]

$$\lambda^2 = \frac{u_{rms}^2}{\langle (\partial_{x_1} u_1)^2 \rangle}, \tag{5.5}$$

where $\langle (\partial_{x_1} u_1)^2 \rangle$ is the ensemble average of $(\partial_{x_1} u_1)^2$ and u_{rms} is the root mean square value of each component of velocity defined as

$$u_{rms}^2 = \frac{2}{3} \int_0^{k_{max}} E(k) dk. \tag{5.6}$$

The time scale of the energy-containing eddies is the large-eddy-turnover time T defined as $T = I/u_{rms}$. The Taylor Reynolds number is

$$Re = \frac{u_{rms}\lambda}{\nu}. \tag{5.7}$$

Forced isotropic turbulence in a periodic box can be considered as one of the most basic numerically simulated turbulent flows. Forced isotropic turbulence is achieved by applying isotropic forcing to the low wave number modes so that the turbulent cascade develops as the statistical equilibrium is reached. Statistical equilibrium is signified by the balance between the input of kinetic energy through the forcing and its output through the viscous dissipation. Isotropic forcing cannot be produced in a laboratory, and therefore forced isotropic turbulence is an idealized flow configuration that can be achieved only via a controlled numerical experiment; nevertheless, forced isotropic turbulence represents an important test case for studying basic properties of turbulence in a statistical equilibrium.

In the statistically stationary state, the average rate of energy addition to the velocity field is equal to the average energy-dissipation rate. The Reynolds number attainable for a given size of simulation is substantially higher for forced turbulence than for the case of decaying turbulence.

We apply forcing over a spherical shell with shell walls of unit width centered at wave number one, such that the total energy injection rate is constant in time. This forcing procedure was used by Misra and Pullin in [27]. The forcing amplitude is adjustable via the parameter δ, while the phase of forcing is identical to that of the velocity components at the corresponding wave vectors. The Fourier coefficient of the forcing term is written as

$$\hat{f} = \frac{\delta}{K} \frac{\hat{u}}{\sqrt{\hat{u}_k \hat{u}_k^*}}, \tag{5.8}$$

where $\hat{f}$ and $\hat{u}$ are the Fourier transforms of the forcing vector and velocity, respectively, and K is the number of wave modes that are forced. The above form of forcing ensures that the energy injection rate $\sum \hat{f} \cdot \hat{u}$ is a constant which is equal to δ. We chose $\delta = 0.1$ for all of our runs. The forcing is added at the large scales ($|\mathbf{k}|$ between 1 and 2).

The DNS is performed by using a 512^3 mesh in a periodic 3D cube of sides $L = 2\pi$. We solve the incompressible Navier–Stokes equations for the velocity field, by using a pseudospectral code. A second order explicit Runge–Kutta scheme is used for time-marching. To eliminate the aliasing error in the pseudospectral method and achieve maximum resolution, we use a 36th order Fourier smoothing function to damp the high frequency modes. Specifically, the smoothing function in this case is given by $\rho(k_i) = \exp(-36(k_i/N)^{36})$ for $|k_i| \leq N$. Compared with the 2/3 dealiasing method, this carefully designed high order Fourier smoothing scheme can resolve significantly more high frequency Fourier modes than the traditional 2/3 dealiasing method for a given resolution; see [14].

5.2.1. DNS results. In our 3D computations, we choose the initial condition as a random field with a spectrum peaked around $|\mathbf{k_p}|$=30. For this initial condition, the equilibrium Taylor Reynolds number is approximately 223, and the Reynolds number based on the integral length scale is 1056. The equivalent viscosity coefficient is $\nu = 0.0005$. To present the results in a nondimensional form, we use the integral length scale I and the root mean square of velocity u_{rms}. Throughout the forced simulations, these two quantities vary significantly; however, as equilibrium is approached, the integral length scale for the simulation approaches the value of approximately $I = 0.56$, and the root mean square of velocity is $u_{rms} = 0.61$. It follows that the corresponding eddy-turnover time is $T = I/u_{rms} = 0.91$. The computations are continued for more than 30 eddy-turnover times. The plots of the total kinetic energy

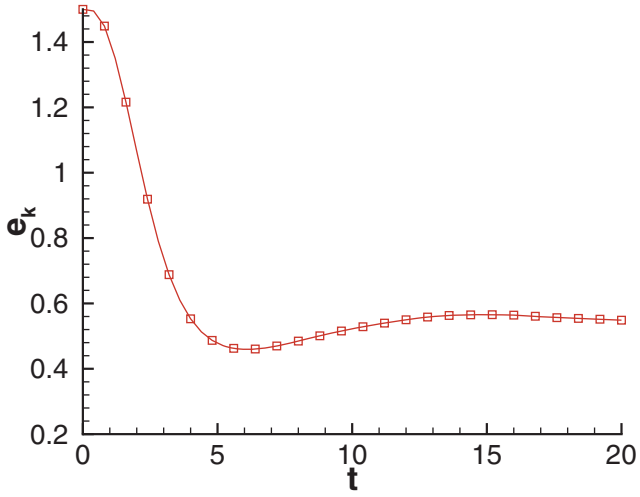

FIG. 5.7. *Temporal evolution of total kinetic energy.*

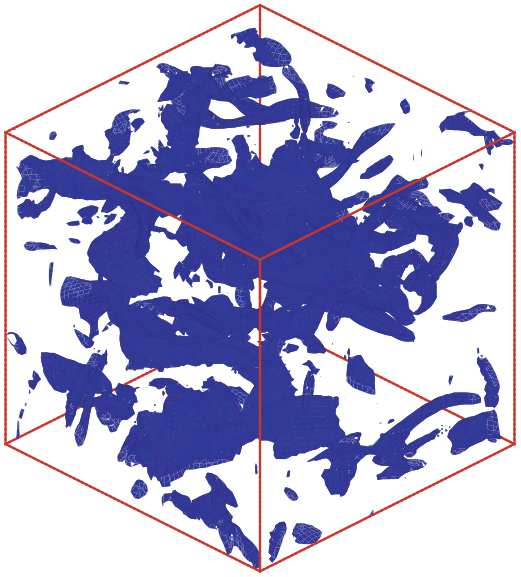

FIG. 5.8. *Isosurface plot of vorticity.*

and energy spectrum indicate that, after 10 eddy-turnover times the flow reaches an equilibrium state; see Figure 5.7. Figure 5.8 shows the isosurface of the magnitude of the vorticity at equilibrium ($t = 30$), at a value two standard deviations above the mean value. The intense vorticity is organized into tubelike structures; see also [19].

5.2.2. Solving the multiscale model. At time $t = 5.0$ of the DNS simulation, small scales have developed due to energy cascade. We use the DNS data at $t = 5$ as the initial condition for the multiscale model and reparameterize the initial condition by using the scheme outlined in section 2.1. By following the numerical algorithm

outlined in section 4.2, we solve the averaged equations for the velocity field:

$$\begin{aligned} &\text{(a)}\quad \bar{\partial}_t \mathbf{u} + (\mathbf{u}\cdot\nabla_x)\mathbf{u} + \nabla_x p + \nabla_x \cdot \langle \mathbf{w}\otimes\mathbf{w}\rangle = \nu\Delta\mathbf{u} + \mathbf{f},\\ &\text{(b)}\quad \nabla_x\cdot\mathbf{u} = 0,\\ &\text{(c)}\quad \mathbf{u}|_{t=0} = \mathbf{U}(\mathbf{x}). \end{aligned} \tag{5.9}$$

In the meantime, we solve the averaged equations for the inverse of the Lagrangian map (we ignore the $O(\epsilon)$ term and apply the high order Fourier filtering to the solution at each time step):

$$\begin{aligned} &\text{(a)}\quad \bar{\partial}_t \boldsymbol{\theta} + (\mathbf{u}\cdot\nabla_x)\boldsymbol{\theta} = \mathbf{0},\\ &\text{(b)}\quad \boldsymbol{\theta}|_{t=0} = \mathbf{x}. \end{aligned} \tag{5.10}$$

For the cell problem, we solve

$$\begin{aligned} &\text{(a)}\quad \partial_\tau \mathbf{w} + (D_x\boldsymbol{\theta}\mathbf{w}\cdot\nabla_z)\mathbf{w} + D_x\boldsymbol{\theta}^\top\nabla_z q - \frac{\nu}{\epsilon}\nabla_z\cdot(D_x\boldsymbol{\theta}D_x\boldsymbol{\theta}^\top\nabla_z\mathbf{w}) = \mathbf{0},\\ &\text{(b)}\quad (D_x\boldsymbol{\theta}^\top\nabla_z)\cdot\mathbf{w} = 0,\\ &\text{(c)}\quad \mathbf{w}|_{\tau=t=0} = \mathbf{W}(\mathbf{x},\mathbf{z}). \end{aligned} \tag{5.11}$$

Since we force only the low wave numbers, the forcing term does not enter the cell equations, which govern the flow of subgrid scales. The energy cascade between the resolved scales and the subgrid scales is caused by the convection terms. In the averaged equations, the effect of small scales influences the large-scale solution through the subgrid stress term $\langle \mathbf{w}\otimes\mathbf{w}\rangle$. The net effect of this term is to dissipate the energy in the large scale. In the cell equations, the large-scale solution is coupled to the small-scale solution through the term $D_z\mathbf{w}D_x\boldsymbol{\theta}\mathbf{w}$.

In principle, the forcing will enter the cell problem through the next order term of order ϵ, which we neglect in this simulation. If we compute the solution for $1/\epsilon$ order in time, this lower order term will be important. Since we compute the cell problem for about five local eddy-turnover times, the correction term can be neglected.

The multiscale analysis provides a multiscale computational method to calculate the Reynolds stress terms from the cell problem. However, for the 3D problem it is not practical to solve the cell equation and take the average on each cell. Instead, we need to design an adaptive numerical scheme that utilizes the homogeneous property of turbulence, i.e. a scheme that captures the large-scale effect of the Reynolds stress by solving the cell equations on a limited number of cells.

5.2.3. Adaptive multiscale model. In this subsection, we will demonstrate that, by using an adaptive strategy, we can compute our multiscale model at a cost comparable to the eddy viscosity model but with better accuracy and without any unknown parameters to be fitted. To design an effective adaptive strategy, we note that, when the turbulent flow field approaches the statistical stationary state, the variation of the Reynolds stress tensor becomes small both in space and in time. Therefore it is not necessary to update every cell problem. Instead, we need only to compute those cells that are disturbed from the equilibrium state. From the cell equation (5.11), we notice that the disturbance to the cell equation comes from the term $D_x\theta$, which represents the influence from the local gradient of the mean flow. If the value of $D_x\theta$ remains constant in time, the cell will stay in the equilibrium stage. However, if the value of $D_x\theta$ changes due to the shearing of the mean flow map, the cell will be disturbed away from the equilibrium stage and will evolve until it reaches a new equilibrium state.

Based on this consideration, we propose an adaptive multiscale model, which we will describe below. At each time step $t = t_n$, we compute the matrix norm $G = \|(D_x\theta)_n^T(D_x\theta)_n - I\|$ on each coarse grid. This term measures the deformation of the unit cell, which represents the magnitude of the local disturbance from the large-scale flow to the subgrid flows. If there is no cell deformation, e.g., a rigid motion, then we have $(D_x\theta)_n^T(D_x\theta)_n = I$. We compare the values of G among all of the coarse grids and update a total of P cells that have the largest value of G. The number of cells to be updated at each time step P is the parameter that controls the accuracy of the multiscale model. When $P = 64^3$, i.e, we update every cell at each time step, the cost of the scheme is the same as the DNS. On the other extreme, if $P = 1$, i.e., we update only one cell in the computational domain, this is equivalent to the eddy viscosity model. In our study, we test $P = 32, 64, 128$. The cell equations are solved with a 32^3 grid, and the averaged equations are solved with a 64^3 grid.

Although we do not need to update every cell solution at each time step, we need to save the flow field of each cell as the initial condition at a later time when that cell needs to be updated. In this case the memory usage is equivalent to a grid of $32^3 \times 64^3 = 2048^3$, which exceeds the capacity of the cluster we use. To alleviate this difficulty, after solving the cell equations and obtaining the Reynolds stress, we save only the first 16 Fourier modes in each direction. When the flow field of a cell needs to be updated, these first 16 modes are used as the initial condition, with higher modes being set to zero. During the computation of the cell equations, the higher modes will grow due to the nonlinear interaction. In addition, the turbulence within a cell has its own time scale, the eddy-turnover time t_{cell}, which is about $1/64$ of the eddy-turnover time of the averaged flow T. Our numerical experiments show that it is enough to solve the cell equations for $5t_{cell}$, and the cell flow field will reach a quasi-equilibrium state. This scheme has substantial savings in the computation time compared with DNS and yet has accuracy comparable with DNS.

Figure 5.9 plots the comparison of energy spectrum at $t = 30.0$. We can see that the energy spectra obtained with $P = 64$ and 128 agree very well with those obtained by the DNS; even with very small cell numbers $P = 32$, the solution agrees well at low wave numbers, and the energy spectrum at the cutoff wave number is higher than the DNS, due to smaller energy dissipation from the small scales.

The comparison in energy spectrum shows only that the subgrid-scale model (SGS) captures the total energy dissipation at the cutoff wave number. It is more important to study basic structural properties of subgrid stresses with respect to the large-scale characteristics of the flow field. A comprehensive knowledge of the fine-scale motions is essential in the development of a proper turbulent theory and any turbulent model. These coherent fine-scale structures have been observed in other types of turbulent flows, such as turbulent mixing layers and turbulent channel flows, where they exhibit similar characteristics.

Three-dimensional measurement techniques have been used to study the alignment of the eigenvectors of actual and modeled components of the subgrid stresses as well as the alignments between eigenvectors of the rate of strain tensor and vorticity vector [21, 32, 20]. The studies confirm that there is a preferred local alignment between the second eigenvector of the rate of strain tensor with the vorticity vector, which was previously observed by using the pointwise DNS data. There is also a preferred relative angle between the most compressive eigendirection of the rate of strain tensor and the most extensive eigendirection of the SGS tensor. By following the previous work of experimental study and LES, we will discuss the statistics of

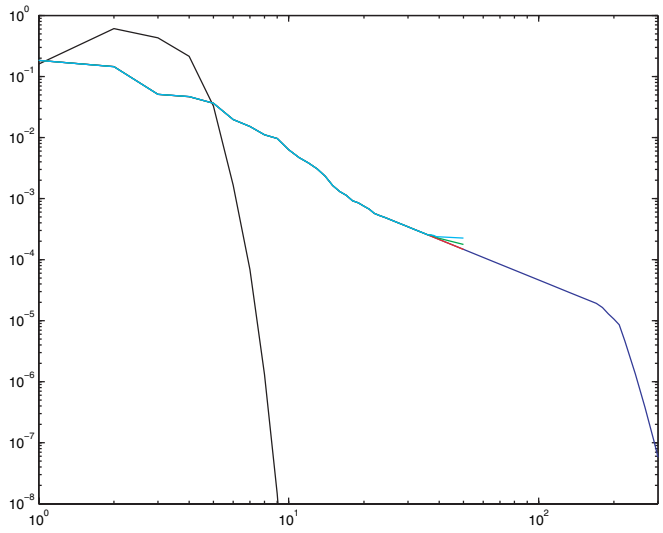

FIG. 5.9. *Comparison of energy spectra. The black curve corresponds to the energy spectrum at* $t = 0$. *The other curves correspond to the energy spectra at* $t = 30$, *which are DNS (blue);* $P = 128$ *(red);* $P = 64$ *(green);* $P = 32$ *(light blue).*

alignment between the eigenvectors of the SGS tensor τ and both the eigenvectors of the rate of strain tensor D and the unit vorticity vector ω.

In the DNS, the mean velocity is obtained by filtering the full velocity field $\mathbf{v}$ with a cutoff filter, and the SGS tensor is defined by

$$\tau_{ij} = \overline{v_i v_j} - \bar{v}_i \bar{v}_j, \tag{5.12}$$

where $\bar{v}_i$ is some low pass filter of v_i. In the multiscale computation, $\tau = \langle \mathbf{w} \otimes \mathbf{w} \rangle$ is obtained by solving the cell equations.

We denote the eigenvectors of D by $[e_1, e_2, e_3]$, ordered according to the corresponding eigenvalues $(\lambda_1, \lambda_2, \lambda_3)$, with $\lambda_1 > \lambda_2 > \lambda_3$. The eigenvectors of τ are (t_1, t_2, t_3) with eigenvalues $(\gamma_1, \gamma_2, \gamma_3)$ such that $\gamma_1 > \gamma_2 > \gamma_3$. Thus, for example, we refer to e_1 as the most extensional eigendirection of D and to t_3 as the most compressive eigendirection of τ.

We first compute the distribution of the energy transfer function $\epsilon_{sgs} = \tau : D$ between the filtered scales and subgrid scales. The segment with $\epsilon_{sgs} < 0$ corresponds to energy backscatter. Figure 5.10 shows that the LES computation with $P = 64$ cells captures the probability density function accurately. The computation with $P = 32$ cells is less accurate; however, it still captures some amount of energy backscattering.

By using the same data sets we compute the distributions of the alignment, represented by the cosine of the angles, between the eigenvectors of the rate of strain tensor and vorticity vector as well as the SGS tensor. Figure 5.11 demonstrates that the probability is the highest when the cosine of the angle between the vorticity vector and the eigendirection of the rate of strain tensor corresponding to the intermediate eigenvalue is close to one. Thus the probability is the highest if the angle between these two vectors is close to zero. This is true for both the DNS and the LES computations. This demonstrates the preferential alignment between the vorticity vector and the eigendirection of the rate of strain tensor corresponding to the intermediate eigen-

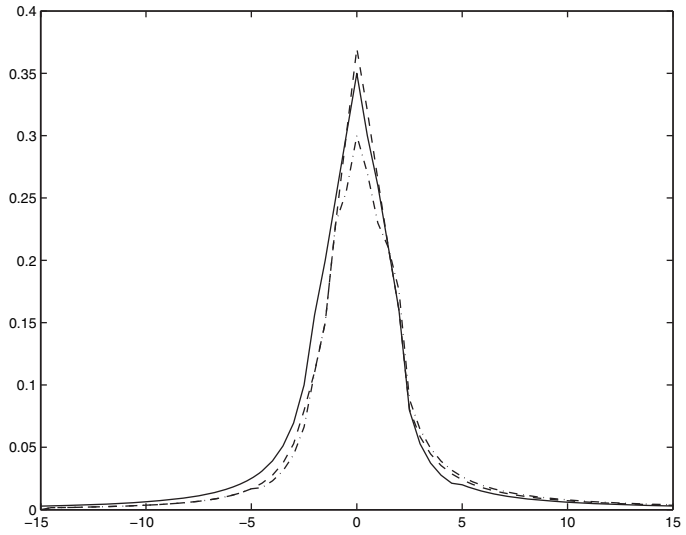

FIG. 5.10. *Probability distribution of $\epsilon_{sgs} = \tau : D$; solid line: forced DNS; dashed line: multiscale model with $P = 64$; dashed-dotted line: multiscale model with $P = 32$. The scaling is based on the energy transfer δ, number of samples N^3, and bin size $\Delta\epsilon_{sgs}$.*

value. In addition, Figure 5.12 presents the alignment between the eigenvectors of the SGS stress tensor and the rate of strain tensor D of the resolved scale. The eigenvectors of the subgrid tensor τ solved from the cell equations display qualitatively similar alignment as that computed from DNS data. We can see that the probability is the highest when the cosine of the angle between e_3 and t_1 is around 0.8. This confirms the experimental observation that there is a preferred angle between e_3 and t_1.

5.2.4. A hybrid Smagorinsky eddy viscosity model. Our multiscale model can potentially give accuracy comparable to the DNS if we solve cell equations on each grid point. As we reduce the number of cells to be solved, the accuracy decreases. In one extreme case, we solve only a few cell problems to obtain one averaged coefficient to be used in the averaged equation. In this case, the coefficient to be computed is the dynamic eddy viscosity, when we assume that the Reynolds stress tensor is aligned with the local rate of strain tensor of the filtered scale [12].

Let $\mathbf{B} = \langle \mathbf{w} \otimes \mathbf{w} \rangle$, which is the SGS. If we assume that the deviatoric part of the SGS tensor is locally aligned with the rate of strain tensor $\mathbf{D}$ of the mean flow, with $\mathbf{D} = \frac{1}{2}(\nabla \mathbf{u} + \nabla \mathbf{u}^T)$ [31, 24, 12, 11], this gives

$$\mathbf{B} = \frac{1}{3} k \mathbf{I} - 2\nu_k \mathbf{D}, \tag{5.13}$$

where $k = \mathrm{tr}(\mathbf{B})$ is the SGS kinetic energy and ν_k the eddy viscosity. The Smagorinsky model [31] can be derived from the $k^{-5/3}$ spectra. This gives

$$k = c_I \Delta^2 ||\mathbf{D}||^2, \qquad \nu_k = c_D \Delta^2 ||\mathbf{D}||, \tag{5.14}$$

where $||\mathbf{D}||$ is the norm of the rate of strain matrix $\mathbf{D}$, defined as

$$||\mathbf{D}||^2 = \sum_{i,j} D_{ij} D_{ij}, \tag{5.15}$$

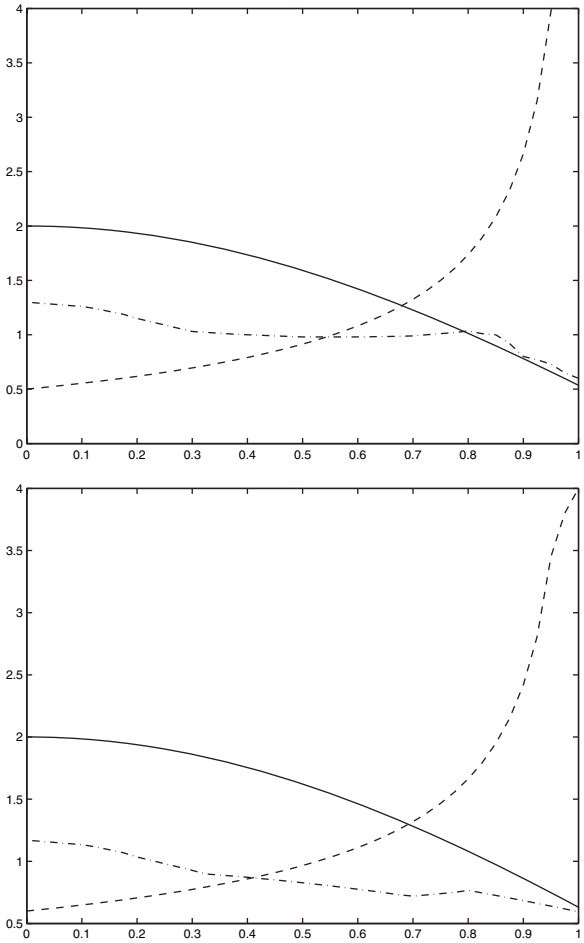

FIG. 5.11. *Probability distribution of $\omega \cdot e_\alpha$ from DNS (the top figure) and the multiscale model (the bottom figure); solid line: $\omega \cdot e_1$; dashed line: $\omega \cdot e_2$; dashed-dotted line: $\omega \cdot e_3$. The x-axis represents the cosine of the angle between the two vectors.*

and Δ is typically taken to be the coarse grid size. For isotropic turbulence, $c_I = 0.404$ and $c_D = 0.042$; see [25].

The weakness of the Smagorinsky model is that the effect of the subgrid flow on the mean flow is always dissipative and is uniform in both time and space. To relax these constraints, the dynamic model of Germano filters the governing equation a second time [12]. By minimizing the residual error throughout the domain, c_I and c_D can be determined dynamically. They vary in time and can be negative but are uniform in space. Numerical simulations show that, at large Reynolds numbers, c_I and c_D become close to 0.4 and 0.04.

By using our multiscale model, we can also design a dynamic model to determine the eddy viscosity. Specifically, c_I can be determined from

$$k = c_I \Delta^2 ||\mathbf{D}||^2 = \mathrm{tr}(\mathbf{B}), \tag{5.16}$$

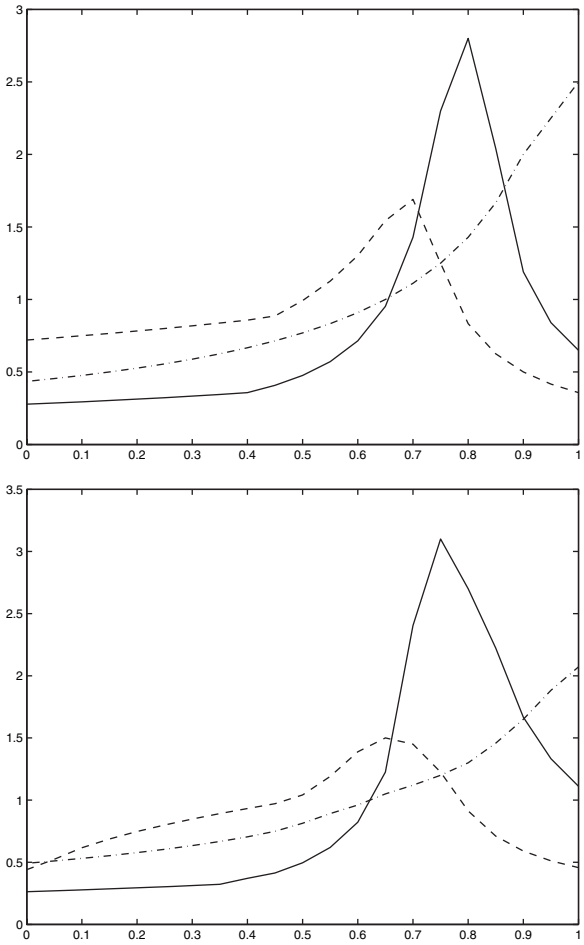

FIG. 5.12. *Probability distribution of $e_\alpha \cdot t_\beta$ from DNS (the top figure) and the multiscale model (the bottom figure); solid line: $e_3 \cdot t_1$; dashed line: $e_2 \cdot t_2$; dashed-dotted line: $e_1 \cdot t_3$. The x-axis represents the cosine of the angle between the two vectors.*

and c_D can be determined by minimizing the error term locally

$$e = \left\| \mathbf{B} - \frac{1}{3}k\mathbf{I} + (2c_D\Delta^2||\mathbf{D}||)\mathbf{D} \right\|. \tag{5.17}$$

This is equivalent to minimizing the quadratic function

$$||e||^2 = 4c_D^2\Delta^4||\mathbf{D}||^2\mathbf{D}^2 + 4c_D\Delta^2||\mathbf{D}||\mathbf{D}B_D + B_D^2, \tag{5.18}$$

where $\mathbf{B}_D = \mathbf{B} - \frac{1}{3}\mathrm{tr}(\mathbf{B})\mathbf{I}$, which leads to

$$c_D = -\frac{\mathbf{B}_D : \mathbf{D}}{2\Delta^2||\mathbf{D}||^3}, \tag{5.19}$$

where $\mathbf{B}_D : \mathbf{D} = \sum_{i,j} B_{ij}D_{ij}$, and $\mathbf{B} = \langle \mathbf{w} \otimes \mathbf{w} \rangle$ is obtained by solving the cell equations. Thus c_I and c_D can vary both in time and in space. In the case of

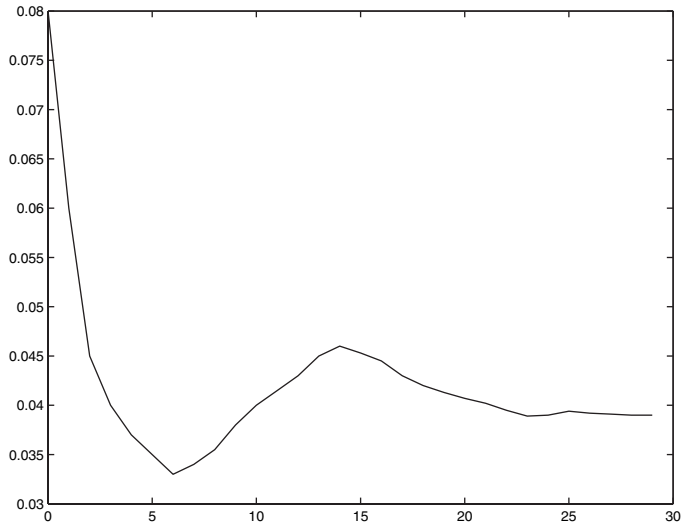

FIG. 5.13. *Temporal evolution of computed eddy viscosity c_D.*

homogeneous isotropic turbulence, we assume that the eddy viscosity is uniform in space. We solve the cell equation at 4 grid points on each dimension, i.e., a total of 64 cells. For each cell we solve on a grid of 32^3. The averaged equation is solved with a grid number of 64^3. On each cell, we calculate c_I and c_D with (5.16) and (5.19), and use (5.14) to compute the SGS kinetic energy k and the eddy viscosity ν_k. The overall eddy viscosity and the SGS kinetic energy are taken to be the average of all cells, and this is plugged into the averaged equation with the Reynolds stress given by (5.13). This process repeats at each large time step. In Figure 5.13, we plot the evolution of c_D. Since the turbulent flow is isotropic and homogeneous, the value of c_I relaxes to the Smagorinsky value of 0.04. In Figure 5.14, we plot the comparison of energy spectra at $t = 30.0$. An inertia range is established which has slope $k^{-5/3}$ [22]. This improved eddy viscosity model shows good agreement with the DNS at the resolved wave numbers.

5.2.5. Comparison of complexity in different multiscale models. Before concluding this section, we make some comparison of complexity among different multiscale models. Let N be the number of coarse grid points along each dimension for both our adaptive multiscale model and the Smagorisky model. Further, we assume that we need to solve for P a number of cell problems by using M number of grid points along each direction. Then the complexity of our adaptive multiscale model is

$$C_{AMS} = N^3 + PM^3.$$

The complexity for the traditional Smagorinsky model is given by

$$C_{LES} = N^3.$$

In a naïve implementation of a dynamic Smagorinsky model, one uses two grids to solve for the Smagorinsky model to determine the eddy viscosity. Therefore, the complexity of a dynamic Smagorinsky model is of the order

$$C_{DLES} = N^3 + (2N)^3.$$

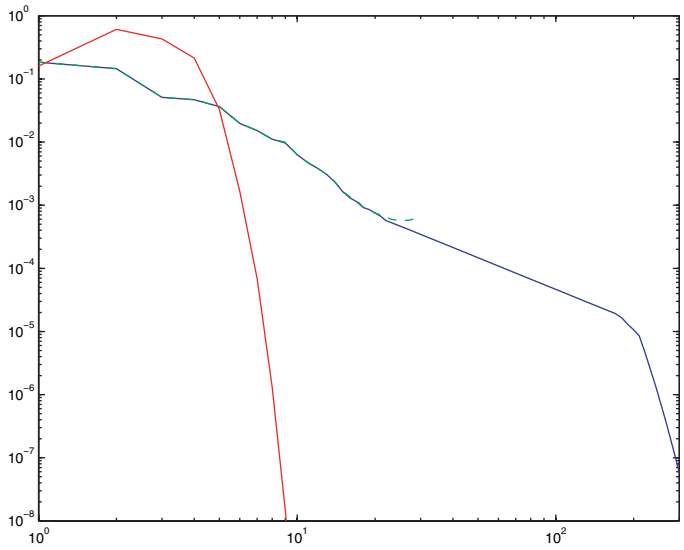

FIG. 5.14. *The comparison of energy spectra between the DNS and the multiscale model. (Solid line) DNS; (red) at* $t = 0$*, (blue) at* $t = 30$*. (Dashed line) Multiscale model at* $t = 30$*.*

Finally, the complexity of a DNS method is of the order

$$C_{DNS} = (N * M)^3.$$

In our numerical experiments, we used $N = 64$, $P = 64$, and $M = 32$. Thus, we have the following comparison of the complexity of various methods:

$$\begin{aligned} C_{DNS} &= (64 \times 32)^3 = 2048^3, \\ C_{AMS} &= 64^3 + 64 * 32^3 = 64^3 + 128^3, \\ C_{LES} &= 64^3, \\ C_{DLES} &= 64^3 + 128^3. \end{aligned}$$

As we can see from the above comparison, our adaptive multiscale model gives a significant savings compared with the DNS. It has the same complexity as the naïve implementation of a dynamic Smagorinsky model but is about 9 times more expensive than the traditional Smagorinsky model.

6. Conclusion and discussion. By using a systematic multiscale analysis, we derived a multiscale model to solve incompressible Navier–Stokes equations. An important feature of our multiscale model is that it does not require any closure assumption and has no unknown parameters. Our numerical experiments demonstrated that our multiscale model not only obtained good agreement with a high resolution DNS result in the energy spectrum and kinetic energy evolution but also correctly captured the higher order turbulence statistics, including the probability distribution function of subgrid energy transfer, correlation between the eigenvectors of the SGS tensor, the rate of strain tensor, and the unit vorticity vector.

We can compare our multiscale model with the available LES models. All LES schemes are based on some assumed correlation about the subgrid stresses and the local rate of strain of the resolved flow. However, the DNS results and more recent high

resolution experimental results did not show any obvious correlation between those two tensors. The advantage of our multiscale model is that the averaged equations and the cell equations are derived directly from the governing equations based on a systematic multiscale analysis, so the mathematical formulation can be justified formally by ignoring higher order terms in the averaged and cell equations.

One of the important contributions in this paper is that we introduce an adaptive strategy which allows us to reduce the number of cell problems to be updated dynamically. This provides us with an adaptive multiscale model at a cost comparable to a dynamic LES model but with better accuracy and no free parameters. Our adaptive strategy takes advantage of some properties of turbulent flows. When the turbulent flow reaches the state of statistical equilibrium, most subgrid scales become statistically stationary; therefore, they do not need to be recalculated. However, due to turbulence intermittency, some subgrid scales will be disturbed by the large-scale flow. We need only to compute those subgrid cells that are disturbed away from the equilibrium. For fully developed turbulent flows, the number of cells that need to be recalculated is relatively small. This is how our adaptive multiscale model saves computation time. We noticed that the large-scale flow disturbs the cell flow through the convection term $D_z\mathbf{w}D_x\boldsymbol{\theta}\mathbf{w}$, and the regions with large value of $D_z\mathbf{w}D_x\boldsymbol{\theta}\mathbf{w}$ coincide with regions of high shears. In our numerical experiments, we solved 64 cells with 32^3 subgrid points and obtained excellent agreement with the DNS results using 512^3 grid points. In effect, the adaptive multiscale model gives a factor of 128 savings in the number of computational points. This shows that our adaptive multiscale model can achieve a level of accuracy comparable to that of DNS but at a cost comparable to that of a dynamic LES model.

Currently, we are investigating the Reynolds stress term and its structure by studying the cell problem carefully. By exploring the intrinsic coupled between the cell problem and the large-scale equation, we would like to characterize the Reynolds stress term in terms of the large-scale solution through its coupling to the term $D_x\boldsymbol{\theta}$, which accounts for the local deformation and shearing due to the mean flow. We remark that there have been some previous efforts in using the MPP techniques and the structure of the Reynolds stress term to construct a more systematic turbulence model; see, e.g., [30, 7, 29].

Appendix. Derivation of the nested multiscale expansion. In this appendix, we will derive the nested multiscale expansion for $\boldsymbol{\theta}^\epsilon$. First, we define the flow map $\mathbf{x}^\epsilon(t,\boldsymbol{\alpha})$ as follows:

$$\text{(A.1)}\qquad \begin{aligned} &\text{(a)}\quad \frac{d\mathbf{x}^\epsilon}{dt} = \mathbf{u}^\epsilon(t,\mathbf{x}^\epsilon),\\ &\text{(b)}\quad \mathbf{x}^\epsilon|_{t=0} = \boldsymbol{\alpha}. \end{aligned}$$

It is easy to show that $\boldsymbol{\theta}^\epsilon$ is the inverse of the flow map $\mathbf{x}^\epsilon$. It is well known that one can express the vorticity field in terms of the flow map as follows [9]:

$$\text{(A.2)}\qquad \boldsymbol{\omega}^\epsilon(t,\mathbf{x}^\epsilon(t,\boldsymbol{\alpha})) = D_\alpha\mathbf{x}^\epsilon(t,\boldsymbol{\alpha})\boldsymbol{\omega}_{int}\left(\boldsymbol{\alpha},\frac{\boldsymbol{\alpha}}{\epsilon}\right).$$

From (A.2), we can see that the small-scale solution in vorticity essentially propagates along its flow map. The effect of vortex stretching is accounted for by the deformation of the Jacobian matrix of the flow map with respect to the Lagrangian variable $\boldsymbol{\alpha}$. By using the Lagrangian formulation, we can see that the microscopic periodic structure

is preserved under the Lagrangian coordinate. This important feature provides us with a critical guideline in performing our multiscale analysis.

Let $\mathbf{x} = \mathbf{x}^\epsilon(t, \boldsymbol{\alpha})$ and $\mathcal{B}^\epsilon = D_x \boldsymbol{\theta}^\epsilon = (D_\alpha \mathbf{x}^\epsilon)^{-1}$. Since the flow is incompressible, the flow map $\mathbf{x}^\epsilon(t, \boldsymbol{\alpha})$ is volume-preserving, i.e., $\det(D_\alpha \mathbf{x}^\epsilon) = 1$. On the other hand, since $D_\alpha \mathbf{x}^\epsilon D_x \boldsymbol{\theta}^\epsilon = \mathcal{I}$ ($\mathcal{I}$ is the identity matrix), we get $\det(\mathcal{B}^\epsilon) = 1$. By direct calculations, we can show that

$$\mathcal{B}^\epsilon = (D_\alpha \mathbf{x}^\epsilon)^{-1} = (\nabla_\alpha \times (x_2^\epsilon \nabla_\alpha x_3^\epsilon),\ \nabla_\alpha \times (x_3^\epsilon \nabla_\alpha x_1^\epsilon),\ \nabla_\alpha \times (x_1^\epsilon \nabla_\alpha x_2^\epsilon)), \tag{A.3}$$

where x_1^ϵ, x_2^ϵ, and x_3^ϵ are the three components of the flow map $\mathbf{x}^\epsilon$. Moreover, in terms of the Lagrangian variable, we have

$$\Delta \boldsymbol{\psi}^\epsilon = \nabla_\alpha \cdot (\mathcal{B}^\epsilon \mathcal{B}^{\epsilon\top} \nabla_\alpha \boldsymbol{\psi}^\epsilon) \tag{A.4}$$

and

$$\nabla_x \times \boldsymbol{\psi}^\epsilon = [(\nabla_\alpha \times (\boldsymbol{\psi}_1^\epsilon \nabla_\alpha x_1^\epsilon + \boldsymbol{\psi}_2^\epsilon \nabla_\alpha x_2^\epsilon + \boldsymbol{\psi}_3^\epsilon \nabla_\alpha x_3^\epsilon)) \cdot \nabla_\alpha]\, \mathbf{x}^\epsilon = D_\alpha \mathbf{x}^\epsilon [\nabla_\alpha \times \big((D_\alpha \mathbf{x}^\epsilon)^\top \boldsymbol{\psi}^\epsilon\big)].$$

Thus, we can express the velocity field $\mathbf{u}^\epsilon$ as

$$\mathbf{u}^\epsilon = \big(\nabla_\alpha \times ((D_\alpha \mathbf{x}^\epsilon)^\top \boldsymbol{\psi}^\epsilon) \cdot \nabla_\alpha\big)\, \mathbf{x}^\epsilon. \tag{A.5}$$

By putting everything together, we can now summarize the stream function-vorticity formulation under the Lagrangian coordinate system. The stream function $\boldsymbol{\psi}^\epsilon$ and Lagrangian map $\mathbf{x}^\epsilon$ satisfy the following coupled system:

$$\begin{aligned} &\text{(a)} \quad -\nabla_\alpha \cdot (\mathcal{B}^\epsilon \mathcal{B}^{\epsilon\top} \nabla_\alpha \boldsymbol{\psi}^\epsilon) = D_\alpha \mathbf{x}^\epsilon \boldsymbol{\omega}_{int}\left(\boldsymbol{\alpha}, \frac{\boldsymbol{\alpha}}{\epsilon}\right), \\ &\text{(b)} \quad \partial_t \mathbf{x}^\epsilon = \big(\nabla_\alpha \times ((D_\alpha \mathbf{x}^\epsilon)^\top \boldsymbol{\psi}^\epsilon) \cdot \nabla_\alpha\big)\, \mathbf{x}^\epsilon, \quad t > 0, \quad \mathbf{x}^\epsilon(0, \boldsymbol{\alpha}) = \boldsymbol{\alpha}\ . \end{aligned} \tag{A.6}$$

By using the stream function-vorticity formulation in the Lagrangian variable, we can treat the nonlinear convection exactly. We now turn the convection dominant transport problem, which is hyperbolic in nature, into an elliptic problem for the stream function and a quasi-linear convection equation for the Lagrangian flow map. The velocity field can be recovered from these two variables. The system (A.6) is a nonlinear coupling system of the elliptic and the transport equations. From this system, we can see that the multiscale periodic structure is convected by the full velocity field. The solution of this system is a periodic function of $\boldsymbol{\alpha}/\epsilon$. This formulation plays a fundamental role in our multiscale analysis.

The objective of our study is to obtain an averaged equation for the well-mixed long time solution of incompressible flow. We look for multiscale expansions in the stream function and the flow map of the form:

$$\begin{aligned} &\text{(a)} \quad \boldsymbol{\psi}^\epsilon(t, \boldsymbol{\alpha}) = \bar{\boldsymbol{\psi}}(t, \boldsymbol{\alpha}, \tau) + \epsilon \widetilde{\boldsymbol{\psi}}(t, \boldsymbol{\alpha}, \tau, \mathbf{y}), \\ &\text{(b)} \quad \mathbf{x}^\epsilon(t, \boldsymbol{\alpha}) = \bar{\mathbf{x}}(t, \boldsymbol{\alpha}, \tau) + \epsilon \widetilde{\mathbf{x}}(t, \boldsymbol{\alpha}, \tau, \mathbf{y}), \end{aligned} \tag{A.7}$$

where $\tau = t/\epsilon$ and $\mathbf{y} = \boldsymbol{\alpha}/\epsilon$, with $\boldsymbol{\alpha} = \boldsymbol{\theta}^\epsilon$. We assume that $\widetilde{\boldsymbol{\psi}}$ and $\widetilde{\mathbf{x}}$ are periodic functions in $\mathbf{y}$ with zero mean.

The expansion (A.7) is along the exact Lagrangian map for both a "slow variable" and "fast variable." For engineering applications, it is more convenient to study the macroscopic behavior of the fluid flow in the Eulerian coordinate for the slow variable. For this reason, we consider a new expansion which uses the Eulerian coordinate

for the large-scale solution but still uses the Lagrangian coordinate to describe the propagation of the small-scale solution. Let $\boldsymbol{\alpha} = \bar{\boldsymbol{\theta}}(t, \mathbf{x}, \tau)$ be the inverse map of $\mathbf{x} = \bar{\mathbf{x}}(t, \boldsymbol{\alpha}, \tau)$, i.e., $\mathbf{x} = \bar{\mathbf{x}}(t, \bar{\boldsymbol{\theta}}(t, \mathbf{x}, \tau), \tau)$. By applying $\bar{\boldsymbol{\theta}}$ to the flow map

$$\mathbf{x} = \bar{\mathbf{x}}(t, \boldsymbol{\theta}^\epsilon, \tau) + \epsilon \widetilde{\mathbf{x}} \left(t, \boldsymbol{\theta}^\epsilon, \frac{t}{\epsilon}, \frac{\boldsymbol{\theta}^\epsilon}{\epsilon} \right),$$

we get

$$\bar{\boldsymbol{\theta}}(t, \mathbf{x}, \tau) = \bar{\boldsymbol{\theta}} \left(t, \bar{\mathbf{x}}(t, \boldsymbol{\theta}^\epsilon, \tau) + \epsilon \widetilde{\mathbf{x}} \left(t, \boldsymbol{\theta}^\epsilon, \frac{t}{\epsilon}, \frac{\boldsymbol{\theta}^\epsilon}{\epsilon} \right), \tau \right).$$

By expanding around $\epsilon = 0$ and using the identity $\boldsymbol{\theta}^\epsilon = \bar{\boldsymbol{\theta}}(t, \bar{\mathbf{x}}(t, \boldsymbol{\theta}^\epsilon, \tau), \tau)$, we obtain

$$\begin{aligned} \boldsymbol{\theta}^\epsilon &= \bar{\boldsymbol{\theta}}(t, \mathbf{x}, \tau) - \epsilon D_x \bar{\boldsymbol{\theta}}(t, \bar{\boldsymbol{\theta}}, \tau) \widetilde{\mathbf{x}} \left(t, \bar{\boldsymbol{\theta}}, \frac{t}{\epsilon}, \frac{\boldsymbol{\theta}^\epsilon}{\epsilon} \right) + \cdots \\ &= \bar{\boldsymbol{\theta}}(t, \mathbf{x}, \tau) + \epsilon \widetilde{\boldsymbol{\theta}} \left(t, \bar{\boldsymbol{\theta}}, \tau, \frac{\boldsymbol{\theta}^\epsilon}{\epsilon} \right). \end{aligned} \tag{A.8}$$

This gives a nested multiscale expansion for $\boldsymbol{\theta}^\epsilon$.

Acknowledgments. We thank Professors George Papanicolaou, Olivier Pironneau, and Dale Pullin for many stimulating discussions and helpful suggestions regarding this work. We also express our gratitude to the referees for their valuable comments on our original manuscript and for suggesting a better norm to use in our adaptive multiscale algorithm.

REFERENCES

[1] K. G. Batchelor, *Computation of the energy spectrum in homogeneous two-dimensional turbulence*, Phys. Fluids Suppl. II, 12 (1969), pp. 233–239.

[2] C. Bègue, B. Cardot, C. Parés, and O. Pironneau, *Simulation of turbulence with transient mean*, Internat. J. Numer. Methods Fluids, 11 (1990), pp. 677–695.

[3] C. Bègue, T. Chacón-Rebollo, D. W. McLaughlin, G. C. Papanicolaou, and O. Pironneau, *Convection of microstructure.* II, Comput. Methods Appl. Sci. Engrg., 6 (1984), pp. 595–606.

[4] A. Bensoussan, J. L. Lions, and G. Papanicolaou, *Asymptotic Analysis for Periodic Structure*, Stud. Math. Appl. 5, North-Holland, Amsterdam, 1978.

[5] T. Chacón-Rebollo and D. Franco-Coronil, *Derivation of the $k - \epsilon$ model for locally homogeneous turbulence by homogenization techniques*, C. R. Acad. Sci. Paris Ser. I, 337 (2003), pp. 431–436.

[6] T. Chacón-Rebollo, D. Franco-Coronil, and F. Ortegón-Gallego, *Homogenization of incompressible flow with helical microstructures*, Adv. Math. Sci. Appl., 1 (1992), pp. 251–300.

[7] T. Chacón-Rebollo and F. Ortegón-Gallego, *On a Rivlin-Eriksen's theorem application to a turbulence model*, Eur. J. Mech. B Fluids, 14 (1995), pp. 557–576.

[8] T. Chacón-Rebollo and O. Pironneau, *Convection of microstructures by incompressible and slightly compressible flows*, in Oscillation Theory, Computation, and Methods of Compensated Compactness, IMA Vol. Math. Appl. 2, Springer, New York, 1986, pp. 1–22.

[9] A. J. Chorin and J. E. Marsden, *A Mathematical Introduction to Fluid Mechanics*, 3rd ed., Springer, New York, 1993.

[10] M. Farge, K. Schneider, and N. Kevlahan, *Non-gaussianity and coherent vortex simulation for two-dimensional trubulence using adaptive wavelet basis*, Phys. Fluids, 11 (1999), pp. 2187–2201.

[11] U. Frisch, *Turbulence: The Legacy of A. N. Kolmogorov*, Cambridge University Press, New York, 1995.

[12] M. Germano, U. Piomell, and P. Moin, *A dynamic subgrid-scale eddy viscosity model*, Phys. Fluids A, 3 (7) (1991), pp. 1760–1765.

[13] W. D. Henshaw, H. O. Kreiss, and L. G. Reyna, *Smallest scale estimates for the Navier-Stokes equations for incompressible fluids*, Arch. Ration. Mech. Anal., 112 (1990), pp. 21–44.
[14] T. Y. Hou and R. Li, *Dynamic depletion of vortex stretching and non-blowup of the* 3*-D incompressible Euler equations*, J. Nonlinear Sci., 16 (6) (2006), pp. 639–664.
[15] T. Y. Hou, D. P. Yang, and H. Ran, *Multiscale analysis in the Lagrangian formulation for the* 2*-D incompressible Euler equation*, Discrete Contin. Dyn. Sys., 13 (2005), pp. 1153–1186.
[16] T. Y. Hou, D. P. Yang, and H. Ran, *Multiscale computation of isotropic homogeneous turbulent flow*, in Inverse Problems, Multi-Scale Analysis and Effective Medium Theory, Contemp. Math. 408, H. Ammari and H. Kang, eds., AMS, Providence, RI, 2006, pp. 111–135.
[17] T. Y. Hou, D. P. Yang, and K. Wang, *Homogenization of incompressible Euler equation*, J. Comput. Math., 22 (2004), pp. 220–229.
[18] T. J. R. Hughes, L. Mazzei, and K. E. Jansen, *Large eddy simulation and the variational multiscale method*, Comput. Vis. Sci., 3 (2000), pp. 47–59.
[19] J. Jimenez, A. A. Wray, P. G. Saffman, and R. S. Rogallo, *The structure of intense vorticity in isotropic turbulence*, J. Fluid Mech., 255 (1993), pp. 65–90.
[20] H. S. Kang, S. Chester, and C. Meneveau, *Decaying turbulence in an active-grid-generated flow and comparisons with large-eddy simulation*, J. Fluid Mech., 480 (2003), pp. 129–160.
[21] M. Kerr, *Higher-order derivative correlations and the alignment of small-scale structures in isotropic numerical turbulence*, J. Fluid Mech., 153 (1985), pp. 31–58.
[22] A. N. Kolmogorov, *Local structure of turbulence in an incompressible fluid at a very high Reynolds number*, Dokl. Akad. Nauk, 30 (1941), pp. 299–302.
[23] R. Kraichnan, *Inertial ranges in two dimensional turbulence*, Phys. Fluids, 10 (1967), pp. 1417–1423.
[24] A. Leonard, *Energy cascade in large-eddy simulations of turbulent fluid flows*, Adv. Geophys., 18 (1974), pp. 237–248.
[25] K. Lilly, *The representation of small-scale turbulence in numerical experiment*, in Proceedings of the IBM Scientific Computing Symposium on Environmental Sciences, 1967, pp. 195–210.
[26] D. W. McLaughlin, G. C. Papanicolaou, and O. R. Pironneau, *Convection of microstructure and related problems*, SIAM J. Appl. Math., 45 (1985), pp. 780–797.
[27] A. Misra and D. I. Pullin, *A vortex-based subgrid stress model for large-eddy simulation*, Phys. Fluids, 9 (8) (1997), pp. 2443–2454.
[28] P. Moeleker and A. Leonard, *Lagrangian methods for the tensor-diffusivity subgrid model*, J. Comput. Phys., 167 (2001), pp. 1–21.
[29] B. Mohammadi and O. Pironneau, *Analysis of the* $k-\epsilon$ *Turbulence Model*, Wiley-Mason, Paris, 1993.
[30] F. Ortegón-Gallego, *Structural properties of the closure terms of the MPP turbulence model*, in Proceedings of the XIth Congress on Differential Equations and Applications/First Congress on Applied Mathematics, University of Málaga, Málaga, 1989, pp. 409–413.
[31] J. Smagorinsky, *General circulation experiments with the primitive equations.* I. *The basic experiment*, Monthly Weather Review, 91 (1963), pp. 99–164.
[32] Tao, J. Katz, and C. Meneveau, *Effects of strain-rate and subgrid dissipation rate on alignment trends between large and small scales in turbulent duct flow*, in Proceedings of the 3rd ASME Fluids Engineering Division Summer Meeting, Vol. 457, 2000, pp. 35–78.